

NEEDLE DETECTION AND LOCALIZATION IN SIMULATED IN-VIVO ULTRASOUND IMAGE
FOR USE IN BREAST BIOPSY

by

NIDHI KHULLAR

Presented to the Faculty of the Graduate School of
The University of Texas at Arlington in Partial Fulfillment
of the Requirements
for the Degree of

MASTER OF SCIENCE IN ELECTRICAL ENGINEERING

THE UNIVERSITY OF TEXAS AT ARLINGTON

December 2011

Copyright © by NIDHI KHULLAR 2011

All Rights Reserved

ACKNOWLEDGEMENTS

I am grateful to a number of people and organizations that helped me to pursue this research. First and foremost, my profound thanks and appreciation are addressed to my advisor Dr. Venkat Devarajan for his encouragement, help and kind support. His invaluable technical and editorial advice, discussions and guidance were a real support to complete this work.

I wish to express my sincere thanks to my thesis committee members Dr. Alan Davis and Dr. R. Stephen Gibbs of the Department of Electrical Engineering, The University of Texas at Arlington. I would like to thank Dr. Balakrishnan Prabhakaran, Professor Department of Computer Science, The University of Texas at Dallas for his collaboration and guidance throughout this work. I thank Dr. Matthew Lewis, Assistant Professor, UT Southwestern Medical School at Dallas for providing all the Ultrasound imaging data for this research.

I would like to thank my colleagues at Virtual Environment Lab for their moral support and assistance whenever required during this research. They played an important role in the successful completion of my work.

Most of all, I would like to thank my family and friends for their constant encouragement and support.

November 15, 2011

ABSTRACT

NEEDLE DETECTION AND LOCALIZATION IN SIMULATED IN-VIVO ULTRASOUND IMAGE FOR USE IN BREAST BIOPSY

Nidhi Khullar, MS

The University of Texas at Arlington, 2011

Supervising Professor: Venkat Devarajan

This thesis addresses needle segmentation in ultrasound images for breast cancer biopsy. The thesis reviews the state-of-the-art in object localization using ultrasound (US) imagery. In particular, principal component analysis, projection based methods (Hough Transform, Radon Transform and Parallel Integral Projection) and model fitting method using RANSAC and work in the field of diffusion filters are reviewed for potential use in a real breast biopsy environment, wherein the US imagery does not have much contrast and the speckle noise content is high. Other image artifacts in these images also mask the needle image.

A new needle localization method called ANDSUI algorithm has been developed with focus on improved localization accuracy and computational complexity especially when the assumption “needle is brighter than background” fails such, in cases like needle is behind dense tissue. The new method and the state of the art methods have been compared to show that ANDSUI algorithm is superior.

TABLE OF CONTENTS

ACKNOWLEDGEMENTS	iii
ABSTRACT	iv
LIST OF ILLUSTRATIONS.....	ix
LIST OF TABLES	xi

Chapter	Page
1. INTRODUCTION.....	1
1.1 Types of Breast Cancer Biopsy.....	1
1.1.1 Fine needle aspiration.....	1
1.1.2 Core needle biopsy	2
1.1.2.1 Stereotactic biopsy.....	2
1.1.2.2 Ultrasound-guided core biopsy	2
1.1.3 Open biopsy or surgical biopsy.....	2
1.2 Drawbacks of the current breast cancer biopsy techniques	2
1.3 System design for breast cancer biopsy	3
1.3.1 Research motivation	3
1.3.2 Biopsy Planning Phase or Initial Setup phase	4
1.3.3 Biopsy phase.....	5
1.3.4 System components.....	5
1.4 Research motivation for our specific problem	5
1.5 Task Definition.....	6
1.6 General Issues	6
2. ULTRASOUND SYSTEMS	8

- 2.1 Transducer 8
 - 2.1.1 Type of Transducers 9
 - 2.1.1.1 Linear Array..... 9
 - 2.1.1.2 Phase Array/Sector 10
- 2.2 Image formation 11
 - 2.2.1 Filtering..... 11
 - 2.2.2 Envelop detection..... 13
 - 2.2.3 Log Compression..... 13
 - 2.2.4 Scan Conversion 14
- 2.3 Imaging modes..... 14
 - 2.3.1 A-mode..... 14
 - 2.3.2 B-mode (Brightness) 15
 - 2.3.3 M-mode 15
 - 2.3.4 Color Doppler 16
 - 2.3.5 Power Doppler 17
- 3. STATE OF THE ART IN OBJECT LOCALIZATION AND SEGMENTATION IN ULTRASOUND DATA. 18
 - 3.1 Hough Transform 18
 - 3.1.1 Standard Hough Transform..... 18
 - 3.1.2 3D Hough Transform (3DHT)..... 19
 - 3.1.3 Randomized Hough Transform (3DRHT) 21
 - 3.1.4 Probabilistic Hough Transform..... 21
 - 3.1.5 Shortcomings of Hough Transform approach 22
 - 3.2 Principal Component Analysis Method 22
 - 3.2.1 2D Ultrasound Image 22
 - 3.2.2 3D Ultrasound Image 24
 - 3.2.3 Shortcomings of Principal component analysis approach 24

3.3 Radon Transform	24
3.3.1 Shortcomings of Radon transform approach	27
3.4 Parallel Integral Projection	27
3.4.1 Shortcomings of Parallel Integral Projection	30
3.5 Model fitting using RANSAC	30
3.5.1 Thresholding	31
3.5.2 Axis localization.....	32
3.5.3 Shortcomings of model fitting approach.....	33
4. DIFFUSION FILTERS FOR SPECKLE RESUCTION	36
4.1 Speckle Model.....	36
4.2 Diffusion Filters.....	37
4.2.1 Physical background of diffusion filters.....	37
4.2.2 Linear Diffusion Filters	38
4.2.3 Nonlinear Diffusion Filter.....	38
4.2.3.1 The Perona–Malik model (Nonlinear isotropic diffusion models).....	38
4.2.3.2 Regularized Perona–Malik model.....	39
4.2.3.3 Nonlinear anisotropic diffusion models	40
4.2.3.4 Anisotropic regularization of the Perona–Malik model for edge enhancement.....	40
5. ALGORITHM FOR NEEDLE SEGMENTATION AND SIMULATIONS	42
5.1 Cropping borders	46
5.2 Nonlinear anisotropic diffusion filter	46
5.2.1 Demonstration of difference between linear and nonlinear anisotropic diffusion.....	47
5.2.2 Effect of Parameters used in the calculations for nonlinear diffusion.....	47

5.2.2.1 Contrast parameter λ	47
5.2.2.2 Speed of diffusivity m	49
5.2.2.3 Space regularization parameter or standard deviation of the Gaussian kernel σ	50
5.2.2.4 Number of steps T	50
5.2.3 Simulation results of linear and nonlinear diffusion filter on US images.	51
5.3 Connected component analysis	54
5.4 Second order Gaussian filter and morphological closure	55
5.4.1 Morphological closing.....	56
5.4.2 Second order Gaussian filter.....	56
5.4.3 Demonstration for results of Morphological closing and 2 nd order Gaussian filter	57
5.5 Needle marking using Hough Transform	57
5.6 Results and Calculation	58
5.6.1 Angle Calculations	58
5.6.2 Length Calculations.....	58
5.6.3 Tip Position Calculations.....	58
6. CONCLUSION AND FUTURE WORK.....	66
6.1 Conclusion	66
6.2 Future Work.....	66
REFERENCES.....	67
BIOGRAPHICAL INFORMATION	73

LIST OF ILLUSTRATIONS

Figure	Page
1.1 Flowchart of new system design	4
2.1 Each element of the transducer array excited by a delayed excitation pulse	9
2.2 (a) Linear array transducer (b) Linear array image of breast cyst (c) Linear array scanning	10
2.3 (a) Phase array transducer (b) Phased array image of breast cyst (c) Sector scanning	10
2.4 Coordinate system for ultrasound imaging.....	11
2.5 Flow diagram representation of the reconstruction of the ultrasound image from received RF signals.....	12
2.6 Envelop detection using Hilbert transform	13
2.7 (a) Raw B-mode image data; before scan conversion (b) B-mode image after scan conversion	14
2.8 Ultrasound images of different modes (a) A-mode image (b) B-mode image (c) M-mode image (d) Color Doppler image (e) Power Doppler image	16
3.1 Example of Radon Transform	26
3.2 (a) Picture (b) ultrasound image of the needle with passive markers.....	26
3.3 (a) Integral of the image intensity function is calculated along a line given by the point $Q [u, v]$ and a vector w . (b) Evaluation of the PIP transformation of a 3-D image.....	28
3.4 Principle of hierarchical mesh-grid algorithm	29
3.5 Statistical models of the intensity distribution. The parameters of four probability distributions were estimated to fit the intensity of training images.....	31
3.6 Parametric cubical curve	32
5.1 Comparison of data set used by some of the researches.....	43
5.2 Flowchart for the Accurate Needle Detection in Speckled US Images algorithm (a) Steps in ANDSUI algorithm	

(b) Initial manual settings.	45
5.3 (a) Original image (b) Binary mask (c) Cropped image after removal of the borders.	46
5.4 Demo to show the difference between linear and nonlinear diffusion. (a) Linear Diffusion (b) Nonlinear diffusion.	47
5.5 Comparison of Diffusivity and Flux with increasing gradient magnitude for $\lambda=10$ (red line) and $\lambda=20$ (blue line).	48
5.6 Effect of increasing λ on US images	49
5.7 Effect of increasing m on Diffusivity and Flux	49
5.8 Effect of increasing σ on US images. From left to right, σ increase from 3 to 20, keeping λ , m and T fixed.....	50
5.9 Effect of increasing T on US images.....	51
5.10 Result of Diffusion filter step. (a) Original Image (b) Linear Diffusion (c) Nonlinear Diffusion with (d) Diffusivity used for nonlinear diffusion.	52
5.11 Colormap images of the diffusion filter step.....	53
5.12 (a) Connected components are marked in a binary image (b) Connected components are labeled.	54
5.13 Result after applying connected component analysis (a) Original Image (b) Linear Diffusion (c) Nonlinear Diffusion with (d) Diffusivity used for nonlinear diffusion.....	55
5.14 Surf of 2 nd order Gaussian filter	56
5.15 Second order Gaussian filter (a) Original image from step nonlinear diffusion (b) Image after passing through the second order Gaussian filter and morphological closure.	57
5.16 False results when borders are not cropped (a) Original image (b) Accumulator array plot of Hough transform (c) Needle segmented marked as red.....	60
5.17 (a) Original image (b) Accumulator array plot of Hough transform (c) Observed needle (d) Needle segmented marked as red.....	61
5.18 (a) Original image(b) Accumulator array plot of Hough transform (c) Observed needle (d) Needle segmented marked as red.....	63
5.19 (a) Original image (b) Accumulator array plot of Hough transform (c) Observed needle (d) Needle segmented marked as red There are also some false markings.....	64

LIST OF TABLES

Table	Page
3.1 Comparison of 3D Hough transform and 3D Randomized Hough transform	21
3.2 Comparison of previous work: Object localization and segmentation	34
5.1 Needle location in terms of angle, length, starting coordinates and ending coordinates for different input images.....	59

CHAPTER 1

INTRODUCTION

“Breast cancer is the most common cancer among American women, after skin cancer. Today, approximately 1 in almost every 8 women (13.4%) develops breast cancer in her lifetime. Breast cancer is the second-leading cause of cancer death in women after lung cancer -- and is the leading cause of cancer death among women ages 35 to 54 [47].” Estimated new cases and deaths from breast cancer among females in the United States in 2011: New cases - 230,480 Deaths - 39,520 [48].

A breast biopsy is a procedure in which part or all of a suspicious breast growth is removed and examined, usually for the presence of cancer. The growth sample is suctioned out through a needle or cut out using a surgical procedure. The sample is then examined and evaluated under a microscope by a pathologist to identify non-cancerous (benign) or cancerous (malignant) tissue.

1.1 Types of Breast Cancer Biopsy

1.1.1 Fine needle aspiration (FNA)

Fine needle aspiration (FNA) is the least invasive method of biopsy. The surgeon uses a thin needle with a hollow center to remove a sample of cells from the suspicious area. If the area to be biopsied can be felt, the doctor locates the lump or suspicious area and guides the needle there. In cases where the lump cannot be felt, the surgeon may need to use imaging studies to guide the needle to the right location. This is called ultrasound-guided biopsy when ultrasound is used or stereotactic needle biopsy when mammogram is used [54]

1.1.2 Core needle biopsy

Core needle biopsy uses a larger hollow needle than fine needle aspiration does because actual breast tissue is removed, rather than a tiny sampling of cells. In most cases, the needle is inserted about 3 to 6 times so that the doctor can get enough samples.

1.1.2.1 Stereotactic biopsy

This kind of biopsy is used to get a tissue sample from a lump that cannot be felt during a breast exam, but can be seen on a mammogram. The surgeon will use a special type of X-ray imaging, to find the lump that the needle must target, in order to get an accurate tissue sample. The needle will follow the X-ray to the area of concern, and take a tissue sample.

1.1.2.2 Ultrasound-guided core biopsy

A biopsy needle is placed into the breast tissue. Ultrasound helps confirm correct needle placement -- using sound waves reflected off breast tissue -- so the exact location of the abnormality is biopsied. Ultrasound can distinguish many benign lesions, such as fluid-filled cysts, from solid lesions.

1.1.3 Open biopsy or surgical biopsy

This surgical technique requires a cut in the skin, in order to remove a sample of the lump, or sometimes, the entire lump. In addition to removing the suspected cancer, the surgeon generally removes a small rim of normal tissue around it as well.

1.2 Drawbacks of the current breast cancer biopsy techniques

Although we have different procedures to conduct breast biopsies, it is difficult to conclude the test in one attempt and multiple incisions are required to extract the exact suspicious tissue. The breast biopsy procedure is an uncomfortable and painful process, needing multiple sittings. Most of the physicians prefer the stereotactic procedure because the visualization and the accuracy of the localization of the cancer cell is excellent. However, stereotactic biopsy makes use of X-Rays which is ionizing radiation. Using Ultrasound is an alternative to X-ray and it gives visualization in real time. However, Ultrasound provides noisy low-resolution images, and

so it is difficult to track the biopsy needle and avoid zones of exclusions which should not be pricked (blood vessels). These situations pose real challenges for the novice doctors, while even experienced physicians can arrive at incorrect conclusions. Also, in all the above procedures the patient is usually made to lie on her stomach, which is uncomfortable for the old patients that suffer from acid reflux.

1.3 System design for breast cancer biopsy

1.3.1 Research Motivation

Doctors who are performing the biopsy on patients welcomed the idea of having some guidance and visualization, while they were performing the procedure on patients. The Virtual Environment Lab (Director: Dr. Venkat Devarajan) at The University of Texas at Arlington developed a haptic guided breast biopsy training system called ViHAB. In ViHAB, the doctor guides the haptic device (to which the needle is attached) to the target cancer tissue along a path calculated by the system. The haptic device gives feedback whenever the doctor tries to deviate from this path, thereby guiding it to the tissue. While this system proved the feasibility of the approach, there were several improvements to be made. For instance, in ViHAB, the doctor would not directly manipulate the needle, but would control the needle remotely by a joystick. This did not correspond to the actual biopsy performed by interventional radiologists, who would directly insert the needle into the tissue. Thus, as a part of a new collaborative effort with Dr Balakrishnan Prabhakaran of The University of Texas at Dallas, VEL developed a newer design. This design (in consultation with interventional radiologist Dr. Kathryn Hall at Baylor Medical Center), will be able to provide doctors guidance and visualization, and also work as a training tool for novice doctors so that they will gain experience without having to perform biopsy on patients.

The imaging technique used needs to be non-ionizing, which leaves us with Ultrasound as the best option. The disadvantage with Ultrasound images is that they are noisy. We still prefer this as the imaging technique because it is a non-ionizing method.

The overall system can be divided into two blocks: Biopsy Planning Phase or Initial Setup and Biopsy Phase as shown in figure 1.1.

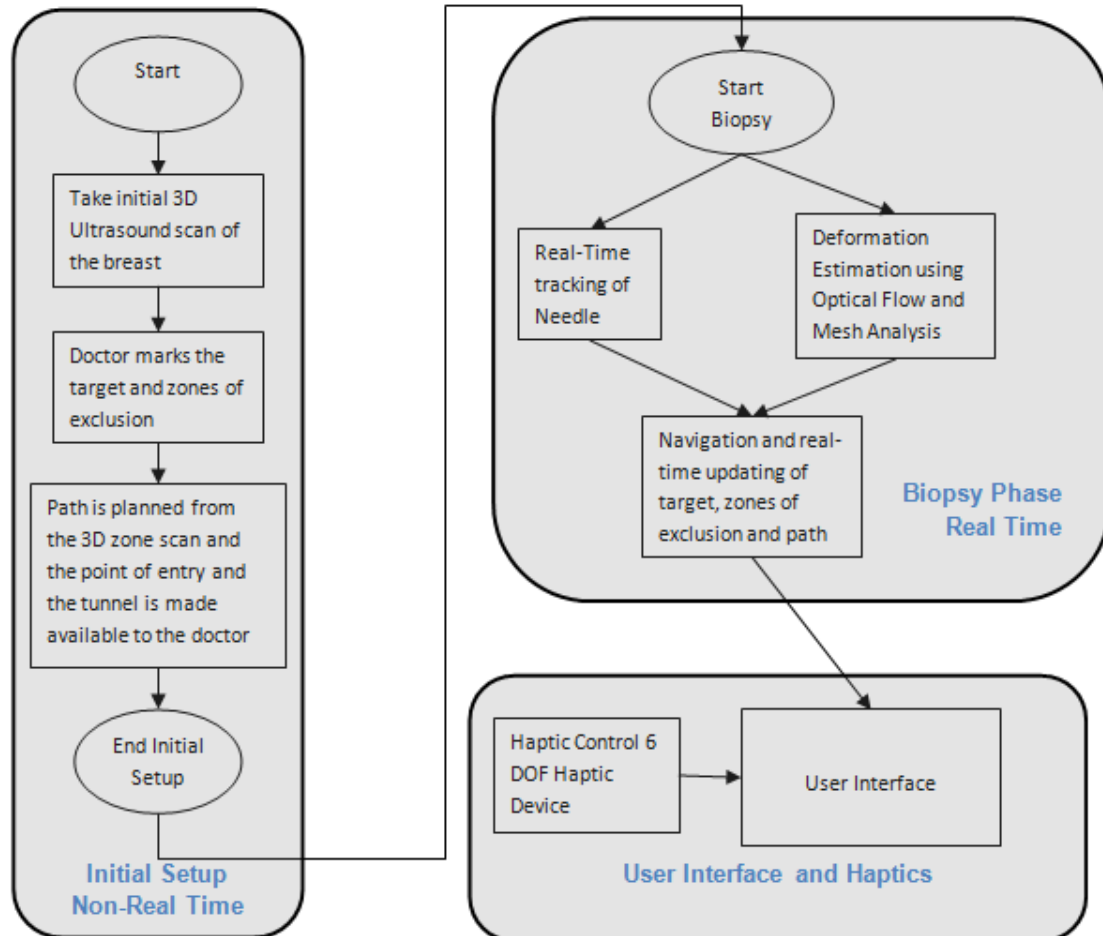


Figure 1.1 Flowchart of new system design

1.3.2 Biopsy Planning Phase or Initial Setup phase

During this phase, the patient is made to sit in a comfortable position on a chair with the surgeon sitting beside her with the ultrasound equipment on the other side. Initially, the surgeon takes a Color Doppler Ultrasound scan of the breast to mark the target and the zones of exclusion. Once these are marked, a mesh of the entire breast is constructed from the

ultrasound data, which is used for deformation tracking. Meanwhile, the 3D ultrasound images are read and the best path from the surface of the breast to the target is determined. Also, an initial point of entry for the needle is provided.

1.3.3 Biopsy phase

This phase is a real time process. Once the path is planned for the doctor by the system, and the deformation tracking and needle tracking systems are initiated, the biopsy is started. The doctor inserts the needle and constantly observes the current position of the needle and the target provided on the user interface. The deformation tracking system tracks the position of the target in real time. The needle tracking algorithm returns coordinates of the needle axis location and tip position in real time. Information from the deformation tracking block and needle tracking block is provided to the path planning algorithm, to recreate a new path if required. Virtual resistance is provided if the doctor deviates from his path.

1.3.4 System components

In this new system design we have following five important components

Visual Imaging (Ultrasound imaging)

Path planning block

Needle tracking block

Tissue deformation tracking block

User interface and Haptic block

1.4 Research motivation for our specific problem

Minimally invasive surgical procedures often involve an insertion of a thin tubular instrument into the human body. For example, in biopsy, tissue samples are taken from a particular region by means of a thin needle [41]. In breast cancer therapy, radioactive substance is injected near the tumor [42]. In all these cases, it is important to localize the instruments for the determination of their precise position. The desired accuracy depends on the application: for needle biopsy, it is of the order of millimeters [43].

The navigation of the needle is vital for reducing the damage to the tissue. Also physician wants to reduce the number of failed insertions.

A number of localization methods have been put into use to allow physicians with a way to know the exact position of the tool at any given time. Initially, a stereotactic frame for instrument guidance was introduced in 1908 [44]. It consisted of a fixed mechanical frame with respect to the patient's body and the object to be tracked. Due to limitation of stereotaxy and patient discomfort, a frameless approach was then proposed: spatial localization of a tool using a radio-frequency signal or optical tracking [45]. In parallel developments in medical imaging CT, MRI, and Ultrasound (US) were also introduced [46]. Here we focus on Ultrasound because of its advantages: there is no ionizing radiation and the cost of ultrasound is modest. Thus our aim is to develop localization method which relies solely on ultrasound data.

1.5 Task Definition

The task addressed in this study is to determine the 2-D position of a needle in an ultrasound image of biological tissue using a fast and robust method. Localization task comprises of two subtasks:

Axis Localization: determination of the axis of the needle

Tip Localization: the actual co-ordinates of the tip of the needle

Localization information can also be used as initialization in an automatic guidance system during a surgical intervention.

1.6 General Issues

There are several impediments to accurate localization. These are enumerated below:

Ultrasound Data Quality: Ultrasound data have low spatial resolution due to large amount of speckle noise. These artifacts make localization task difficult.

Incomplete Object Structure: Sometimes the boundary of a needle in an image is distorted. Also, there are reverberations in the US image as needle is a strong reflecting object. So it is often difficult to find tip of needle.

Computational Cost: We need to localize the needle in real time in order to help with the real time movement of the needle during the actual surgery. So, computational complexity of algorithm must be low.

View Dependency: The appearance of a tool in an ultrasound image depends upon the tool's angle with respect to ultrasound probe. As the experienced surgeon holds the US scanner in his left hand, he "just knows" how to position the scanner with respect to the tip of the surgical needle in his right hand. This is a complex mental/physical co-ordination task that is difficult to teach to the surgical residents and is even more difficult to consistently model in a simulation environment.

CHAPTER 2

ULTRASOUND SYSTEMS

Medical ultrasound is a diagnostic modality permitting view of anatomical structure of organs. Major applications of medical ultrasound can be found in obstetrics to assess fetal health, in cardiology to diagnose heart function and in general diagnostics to investigate inner organs such as liver, kidney and breast. Its popularity arises from the fact that it provides high-resolution images without the use of ionizing radiation. Ultrasound imaging uses the transmission and reflection of high frequency longitudinal sound waves in tissue. Typically, the frequencies used in medical practice range from 1 to 20 MHz. A US image is formed by the received waves reflected from the surfaces between different tissues. The reflection is due to differences in acoustic properties of the tissue. The electrical/mechanical energy conversion required to generate/detect ultrasound waves uses the piezoelectric effect.

2.1 Transducer

The transducer is a key component of an ultrasound system. It acts as a converter of the electrical signal to the mechanical energy and vice versa. In transmission, the transducer excited by a short electric pulse generates mechanical vibrations, which are transmitted into the body as a sound wave (figure 2.1). Subsequently, the transducer operating in a reception mode converts the received sound waves into electrical signals which are processed and displayed as an ultrasound image.

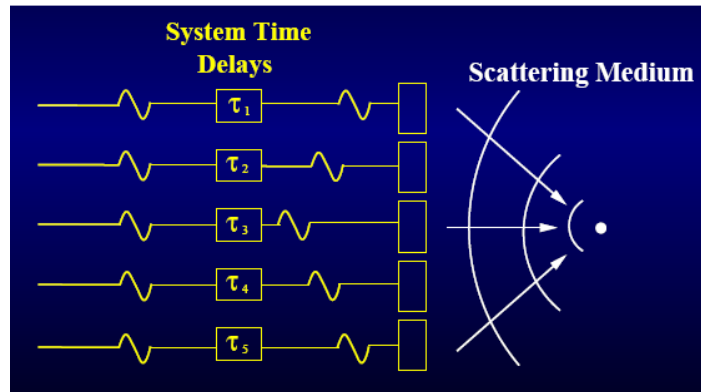


Figure 2.1 each element of the transducer array excited by a delayed excitation pulse [4].

Most transducers are composed of an array of small piezoelectric crystals [1]. The physical layout of crystals on the transducer determines the size of the field of view (FOV) and its dimensionality (2D or 3D).

2.1.1. Type of Transducers

2.1.1.1 Linear Array

A linear transducer consists of a large number (64 – 512) of piezoelectric crystals, arranged linearly. Applying a voltage pulse to a small number of adjacent crystals, a thin sound beam is produced. After all the backscattered echoes have been received by the same subgroup of crystals, a second voltage pulse is applied to the neighboring elements, creating a beam displaced laterally with respect to the first beam [2]. This type of imaging produces rectangular 2D images (Figure 2.2).

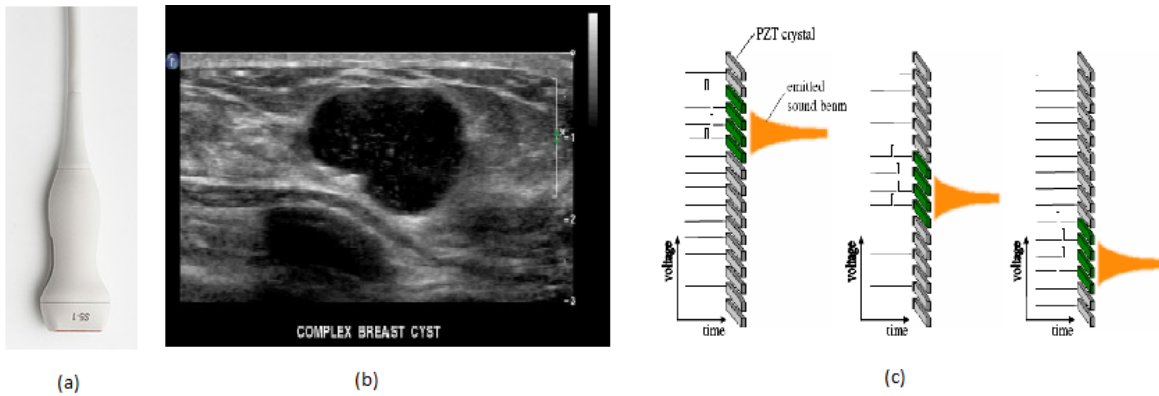


Figure 2.2 (a) Linear array transducer (b) Linear array image of breast cyst (c) Linear array scanning; a small number of adjacent crystals is excited with electrical pulses [1, 4, 6].

2.1.1.2 Phase Array/Sector

The voltage pulse exciting each piezoelectric crystal of sector transducer is delayed in time with respect to each other (Figure 2.3). The sound waves from all piezoelectric elements interact with each other creating a thin, focused beam. The advantage of a phased array probe is that the small footprint allows for imaging in difficult locations [2]. The disadvantage is poor near field resolution.

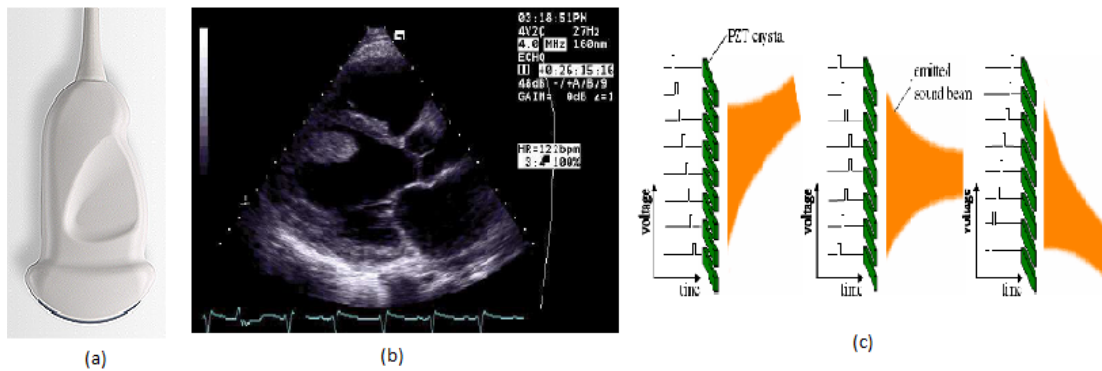


Figure 2.3 (a) Phase array transducer (b) Phased array image of breast cyst (c) Sector scanning; Electric pulses applied to crystals are time-delayed to steer and focus emitted sound beams [1, 4, 6].

2.2 Image Formation

The transducer, in transmission mode is excited by a short electric pulse and generates a sound impulse that is transmitted into the body in a narrow beam. At boundaries between organs and tissue in-homogeneities, a small portion of the wave energy is backscattered in the direction of the transducer. Received waves are converted into electrical signal by the same transducer that has been switched into reception mode. After all echoes have been received along one scan line, the beam is steered to acquire data along another direction [1, 4].

Let N_b be number of ultrasound beams in a scan plane and let θ be the total tilt angle of the scan planes (figure 2.4). The scanner provides for each ultrasound beam a discrete 1D signal that corresponds to the RF signal received from the particular direction.

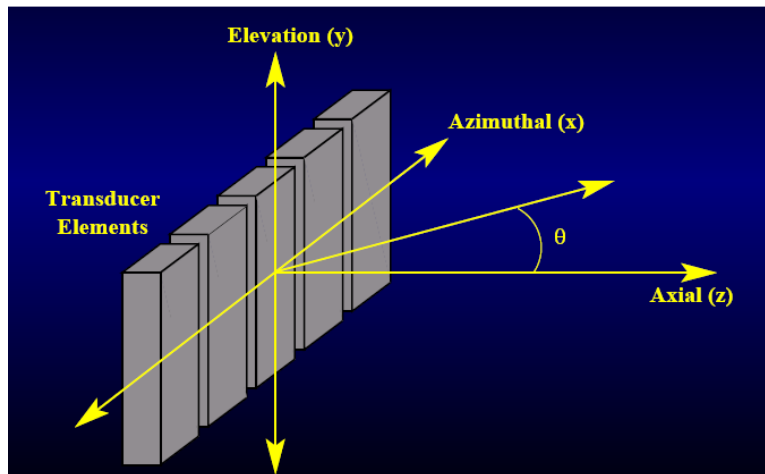


Figure 2.4 Coordinate system for ultrasound imaging [4]

2.2.1 Filtering

Received RF signals will have noise frequency components outside the frequency band of the transducer. So, typically RF signals are filtered with a band-pass filter to reduce noise outside the frequencies of interest (figure 2.5).

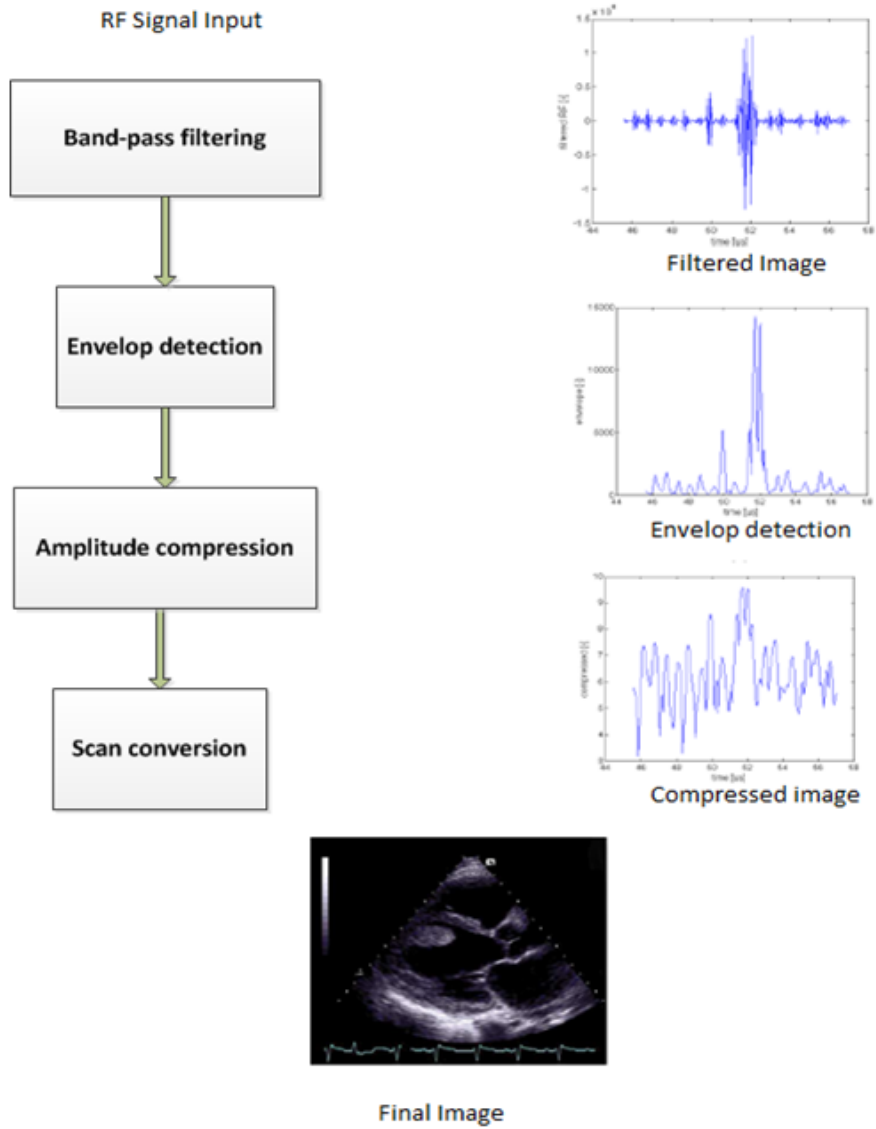


Figure 2.5 Flow diagram representation of the reconstruction of the ultrasound image from received RF signals [1]

2.2.2 Envelop detection

Ultrasound imaging is typically accomplished non-coherently on the envelope of the signal. This envelope extraction process is commonly called detection in ultrasound terminology. Generally, this is performed by creating an analytic representation of the RF signal using Hilbert transform. Hilbert transform is given by equation 2.1

$$H\{u(t)\} = \frac{1}{\pi} \int_{-\infty}^{\infty} \frac{u(\tau)}{t - \tau} d\tau . \quad (2.1)$$

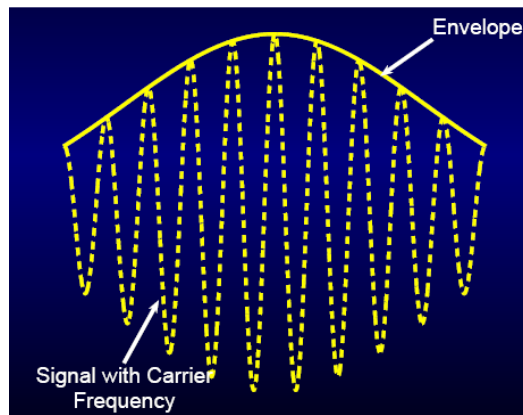


Figure 2.6 Envelop detection using Hilbert transform [4]

The amplitude envelope $e(t)$ of a signal $x(t)$ is computed as the complex module of the sum of the original signal and its Hilbert transformation (figure 2.6). The advantage of this operation is that it is independent of the actual frequency of the operating frequencies and independent of the imaging mode (conventional versus harmonic), or changes in the center frequencies with time.

2.2.3 Log Compression

The maximum dynamic range of the human eye is in the order of 30 dB. The actual dynamic range of the received signal depends on the A/D conversion bits and the depth of penetration

[1]. The signal is compressed to fit the dynamic range used for display (usually 7 or 8 bits). It is typical to use a log compressor to achieve the desired dynamic range for display.

2.2.4 Scan Conversion

This is traditionally the stage at which interpolation between envelope-detected signal lines occurs, to determine the echo amplitude values to be displayed. B-mode (See next section for an explanation of B-mode) images are stored in polar coordinates form. Thus, a scan conversion is needed to transform the polar coordinate data into standard Cartesian coordinates that are needed by standard graphics subsystems (figure 2.7). Generally, the algorithm computes the interpolated points based on their neighbors. Bilinear interpolation is the most commonly used technique for scan conversion [7].

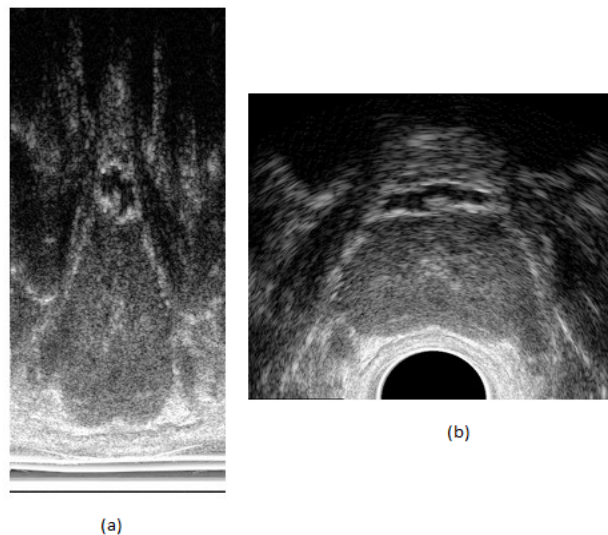


Figure 2.7 (a) Raw B-mode image data; before scan conversion (b) B-mode image after scan conversion [1]

2.3 Imaging Modes

2.3.1 A-mode

This is now an obsolete mode in medical imaging. Wave spikes are represented when a single beam passes through objects of different consistency and hardness. The distance between

these spikes (for example A and B) can be measured accurately by dividing the speed of sound in tissue (1540 m/sec) by half the sound travel time (figure 2.8 (a)).

2.3.2 *B-mode (Brightness)*

Brightness is used to represent the amplitude of the sampled signal. B mode imaging is performed by sweeping the transmitted sound wave over the plane to produce a 2D image (figure 2.8 (b)). Typically, multiple sets of pulses are generated to produce sound waves for each scan line, each set of pulses are intended for a unique focal point along the scan line [3,5,6].

2.3.3 *M-mode*

M-mode refers to scanning a single line in the object and then displaying the resulting amplitudes successively [3]. This shows the movement of a structure such as a heart. Because of its high pulse frequency (up to 1000 pulses per second), this is useful in assessing rates and motion and is still used extensively in cardiac and fetal cardiac imaging (figure 2.8 (c)).

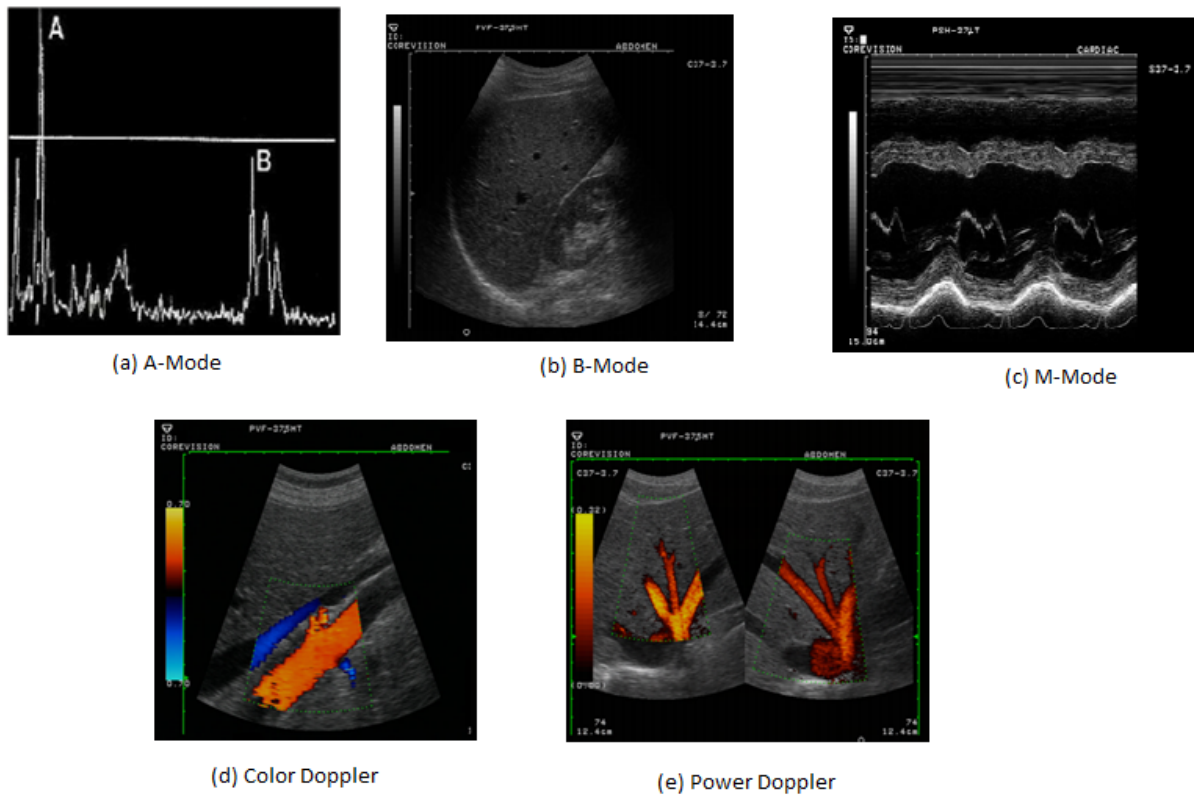


Figure 2.8 Ultrasound images of different modes (a) A-mode image (b) B-mode image (c) M-mode image (d) Color Doppler image (e) Power Doppler image [6]

2.3.4 Color Doppler

In this mode, several pulses are transmitted along each scan line and the Doppler frequency is estimated from the relative time between the received signals [3, 5, 6]. Since pulses are used for the signaling, the velocity location can also be determined. This is used to create a color image that is super-imposed on top of the B-mode image. A color code is used to denote the direction and magnitude of the flow ((figure 2.8 (d)). Red typically denoted flow towards the transducer and blue denotes flow away from it. A darker color usually denotes a larger magnitude while a lighter color denotes a smaller magnitude.

2.3.5 Power Doppler

In this mode, the strength or the power of the motion is estimated and displayed, instead of estimating the actual velocity of the motion as in Color Doppler [3, 5, 6]. It is useful to display small motion. There is no directional information in this measurement ((figure 2.8 (e)).

CHAPTER 3

STATE OF THE ART IN OBJECT LOCALIZATION AND SEGMENTATION IN ULTRASOUND DATA

Ultrasound (US) image segmentation is strongly influenced by the quality of data. There are characteristic artifacts in the image, which make the segmentation task complicated such as attenuation, speckle, shadows, and signal dropout; due to the orientation dependence of acquisition that can result in missing boundaries. Further complications arise as the contrast between areas of interest is often low. This chapter attempts to provide a brief review of the approaches that were proposed to solve the task of object localization and segmentation in ultrasound data.

3.1 Hough Transform

3.1.1 Standard Hough Transform

Hough Transform [9] was proposed for detection of lines in 2D images using a voting algorithm. It represented a line in the image space, as a point (a, b) in the parametric space (also known as Hough Space)

$$\text{Line}_{a, b}: \{(x, y) \in \mathbb{R}^2 \mid y = ax + b\}_{\text{Image}} \quad (3.1)$$

Each point (x, y) in the image space is transformed into a set of possible line parameters (a, b) , such that a line $\text{Line}_{a, b}$ passes through (x, y) , which is a line in Hough space. The intersection of all such lines in Hough space is a single point $(a, b)_{\text{Hough}}$ and represents the desired line in the image space:

$$\text{Point}_{x, y}: \{(a, b) \in \mathbb{R}^2 \mid y = ax + b\}_{\text{Hough}} \quad (3.2)$$

The lines can be detected as local peaks in the Hough space.

Line parameterization is now accomplished using polar coordinates, because it avoids the singularity of line parallel to Y-axis.

$$\text{Line}_{a,b} : \{(x, y) \in \mathbb{R}^2 \mid y \sin \theta + x \cos \theta = r\}_{\text{Image}} \quad (3.3)$$

The following properties are considered for Picture plane to parameter plane transformations [9]:

A point in the picture plane corresponds to a sinusoidal curve in the parameter plane.

A point in the parameter plane corresponds to a straight line in the picture plane.

Points lying on the same straight line in the picture plane correspond to curves through a common point in the parameter plane.

Points lying on the same curve in the parameter plane correspond to lines through the same point in the picture plane.

The steps in the implementation of standard Hough transform are as follows:

Specify the acceptable error in θ and r and quantize the θ - r plane into a quadrated grid. The quantized region is treated as a two-dimensional array of accumulators. For each point (x_i, y_i) in the picture plane, the corresponding curve given by (3.3) is entered in the array by incrementing the count in each cell along the curve. Thus, a given cell in the two dimensional accumulator eventually records the total number of curves passing through it. After all figure points have been treated, the array is inspected to find cells having high counts.

3.1.2 3D Hough Transform (3DHT)

3D Hough Transform is an extension of 2D Hough Transform assuming that the approximate needle position and orientation are known either from the manual insertion or the 3D US imaging system [11]. Also, this a priori knowledge is used to discard portions of the 3D US image, which do not contain the needle, thereby reducing the amount of data to be processed.

A straight line in Euclidean 3D space can be defined in terms of a point and an orientation [11], [12]. Each of these components can be represented as 3-tuple over real numbers: the point $p =$

(p_x, p_y, p_z) as the Cartesian coordinates of the position of a point, and the orientation $b = (b_x, b_y, b_z)$ as the direction cosines with respect to the coordinate axes x, y and z . Then, a line in 3D space can be represented as:

$$\text{Line}_{\Phi, \rho, \theta, r} : [x(t), y(t), z(t)] = p_{\theta, r} + t b_{\Phi, \rho} \quad (3.4)$$

Where point $p_{\theta, r}$ is an intersection of line with base plane (intercept point with plane xy). The polar coordinates for $p_{\theta, r}$ and azimuth and elevation for $v_{\Phi, \rho}$ are:

$$p_{\theta, r} = [r \cos(\theta), r \sin(\theta), 0], v_{\Phi, \rho} = [\cos(\Phi) \cos(\rho), \sin(\Phi) \cos(\rho), \sin(\rho)] \quad (3.5)$$

Lines are detected as in 2D HT by using a 4D accumulator is used.

The steps in the implementation of a line in 3D space are as follows:

Create a set D of all edge points of a 3D image.

Determine the proper threshold according to the histogram of the 3D image, and convert the original 3D image into a binary 3D edge image.

Calculate the Hough parameter accumulator $H(\Phi, \theta, \rho, \alpha)$.

The ranges of 3D line parameters can be further decreased if the approximate needle position and orientation are known.

Initialize $H(\Phi, \theta, \rho, \alpha)$ with zeros.

For each 3D edge point (x, y, z) , calculate all possible parameters $(\Phi, \theta, \rho, \alpha)$ using the 3D line's equations, and accumulate the $H(\Phi, \theta, \rho, \alpha)$.

Detect the global maximum cell H_{max} in the $H(\Phi, \theta, \rho, \alpha)$. $(\Phi_{max}, \theta_{max}, \rho_{max}, \alpha_{max})$ will be the parameters of the needle in the 3D image

Bhattacharya [14] proposed decomposing the finding of a line in 3D into first finding the slope of 3D line in 2D parameter space (Φ, ρ) and subsequently finding its intercept of 3D line also in 2D parameter space.

This approach requires a priori knowledge of the orientation and position of the needle to discard portions of the 3D US image which do not contain the needle. Also, in this work an assumption was made that needle has a high gray value.

3.1.3 Randomized Hough Transform (3DRHT)

Xu and Oja [15, 16] proposed Randomized Hough Transform (RHT). The RHT maps a pair of points $(x_1, y_1), (x_2, y_2) \in \mathbb{R}^2$ (which define a line), into a single point (a, b) in the parameter space \mathbb{R}^2

$$\text{Points: } \{(x_1, y_1), (x_2, y_2)\}_{\text{Image}} \rightarrow (a, b)_{\text{Hough}} \quad (3.6)$$

(In contrast to the standard HT, which maps point (x, y) to a curve in a parameter space)

The RHT randomly iteratively samples a random pair of points in a thresholded image and increments corresponding bins in the accumulator. The solution candidates are found to be local maxima in the accumulator. RHT has been generalized in 3D [10, 16] and is used for needle detection. The improved Quick RHT (QRHT) uses a coarse to fine strategy to improve the speed.

Table 3.1 Comparison of 3D Hough transform and 3D Randomized Hough transform [12]

Method	Angle deviation	Length deviation	Time	Memory
3DHT	1.30 ⁰	1.26 mm	3.03 s	2.27 Mb
3DRHT	2.62 ⁰	2.39 mm	0.10 s	0.13 Mb

3D Hough transform is more accurate in terms of needle angle and length deviation compared to 3D randomized Hough transform but later is more efficient in terms of time and memory consumption (Table 3.1).

3.1.4 Probabilistic Hough Transform

In Probabilistic Hough transform [17] a subset of points selected at random is used as input for the Standard Hough transform. The time complexity of PHT is decreased in comparison to Standard Hough transform at the expense of increased variance.

3.1.5 Shortcomings of Hough Transform approach

Hough transform is a time and memory consuming process especially for a large data set. For 3D images, even with the different implementations of the algorithm to make the process efficient, this approach is not cost effective.

Also, Hough transform cannot locate the needle, if its intensity is lesser than the background or if its boundaries are distorted. This algorithm will only work with the assumption that needle's appearance in the image is a straight line.

3.2 Principal Component Analysis Method

Principal component analysis (PCA) is a mathematical procedure that uses an orthogonal transformation to convert a set of observations of possibly correlated variables into a set of values of uncorrelated variables called principal components. The number of principal components is less than or equal to the number of original variables. First principal component has as high a variance as possible and each succeeding component in turn has the highest variance possible under the constraint that it be orthogonal to (uncorrelated with) the preceding components.

3.2.1 2D Ultrasound Image

The first variance I_1 of the image is created from original ultrasound image I_0 to enhance tool voxels and suppress background noise [18].

$$I_1(i,j) = \sum_{k=1}^N \sum_{l=1}^N \frac{[I_0(k,l) - I_{mean}]^2}{N^2} \quad (3.7)$$

$$\text{where, } I_{mean} = \sum_{i=1}^N \sum_{j=1}^N \frac{I_0(i,j)}{N^2}$$

The variance kernel is an area of $N \times N$ pixels, where N is odd, centered on the pixel to be replaced. This process emphasizes the needle, making it appear larger in the image and smoothes the background speckle to provide a more uniform background.

Then a binary image is created by adaptively thresholding the variance image to approximately classify electrode and background pixels. The intensity of variance image is modeled as a single normal distribution with mean μ and variance σ^2 that are estimated from training data. Then threshold T is determined by:

$$T = \mu + k \sigma \quad (3.8)$$

For a small value of k , other background pixels above the threshold will be maintained along with the needle pixels, leading to difficulties in separating the needle from pixels outside the needle region. However, for large k , an image would result in which none of the needle pixels are maintained, leading to errors in its position and orientation measurements.

$$I_2(i,j) = \begin{cases} 255 & \text{if } I_1(i,j) > T \\ 0 & \text{if } I_1(i,j) \leq T \end{cases}$$

To smooth the needle contour, morphological closure with a 3x3 symmetrical structuring element is applied.

A cluster C_i is defined as a group of pixels connected within the 8-pixel neighborhood. Each cluster of pixels is processed using the principal component analysis to determine the best fitting straight line in terms of the least mean squares criterion. Let us denote by R_i the covariance matrix of pixel coordinates in the cluster C_i .

$$R_i = \begin{pmatrix} \sigma_{xx}^2 & \sigma_{xy}^2 \\ \sigma_{yx}^2 & \sigma_{yy}^2 \end{pmatrix} \quad (3.9)$$

where, $\sigma_{xy} = \frac{\sum_{i=1}^B (x_i - x_{mean})(y_i - y_{mean})}{B}$, B is the number of pixels in the cluster

The first and second eigenvectors of the covariance matrix represent the directions in which the variance is minimized and maximized respectively, and can be used to define an ellipse [21]. The line is determined by the eigenvalue corresponding to the highest eigenvector. This was tested by the authors on a cryogel phantom with a breast biopsy needle (2.1 mm in diameter). A phantom is a physical simulation of an organ, in this case the human breast, using animal tissue, gels etc. Targets, to represent cancer cells are placed in this phantom. In this case, the

phantom was scanned with a 2D ultrasound scanner operating at 5.5 MHz. Results of the experiment to localize the biopsy needle using this PCA method show the algorithm has an accuracy of 1 mm for a depth of insertion greater than 15 mm.

3.2.2 3D Ultrasound Image

Novotny [19] extended Draper's [18] method to 3D. 3D data is pre-segmented using thresholding. Thereafter, connected components (using a 26-voxel neighborhood) are analyzed by PCA. The longest and the straightest candidate is selected by maximizing the ratio of the first and second eigenvalue. The test is performed with a cylindrical rod with 6.2mm in diameter submerged in a water tank. It indicates a mean tip accuracy of 0.7 mm with a standard deviation of 0.6 mm.

3.2.3 Shortcomings of the Principal Component Analysis approach

Experiments were conducted only for the small range of angles 0° – 13.1° of needle axis. For this range of angles, the contrast between the needle and the background is high. Segmentation may not be successful at larger angles, where the contrast between the needle and the background is reduced, and thus the contrast in the variance image is also reduced [18].

During the PCA step, the needle cluster is determined to be the cluster that has the longest major axis. This isolates the needle from the background for the ideal data set considered in these papers, wherein the needle is the only structure in the image. However, in an in vivo situation, the images would contain other specular reflectors and scattering structures, which can interfere with the segmentation of needle.

Also, there are possibilities of classifying a wrong cluster to be the needle cluster, when only a small part of the needle appears in the image and, thus does not have a long major axis.

3.3 Radon Transform

The Radon transform maps an image I , into the Radon space $R\{I\}$ wherein 'd' and ' ϕ ' define a line in two dimensions by its perpendicular distance to the origin and slope, respectively. 's' is a free parameter that corresponds to a specific point on the shape.

$$R\{I\}(d, \phi) = \int I(d \cos(\phi - s \sin(\phi)), d \sin(\phi) + s \cos(\phi)) ds \quad (3.10)$$

This can also be extended to 3D [20]. Points on a parametric shape are defined by the function $c(s, p)$ where p defines the parameters of the shape. A line is represented by the midpoint of the line (x_0, y_0, z_0) , angular parameters (θ, Φ) and the length of line L .

Points lying on a line segment are now defined for p and s as:

$$C(s, p) = \begin{bmatrix} x_0 \\ y_0 \\ z_0 \end{bmatrix} + \begin{bmatrix} \cos(\theta) \cos(\Phi) \\ \sin(\theta) \cos(\Phi) \\ \sin(\Phi) \end{bmatrix} * L/2 * s \quad \text{where } s \text{ belongs to } [-1, 1] \quad (3.11)$$

And the Radon Transform can be written as:

$$R_{c(s,p)\{I\}}(p) = \int_{-1}^1 I[C(s, p)] \cdot ds \quad (3.12)$$

Identifying lines in the 3D volume now becomes a problem of finding local maximums of $R_{c(s,p)\{I\}}(p)$ from equation 3.12. The image volume I , along a direction defined by (θ, Φ) is integrated through the point (x_0, y_0, z_0) and the maximum of R is identified.

For e.g. in above figure 3.1 c contains points with a high integral and so the image is brighter than the other four images (with maximum integral value R)

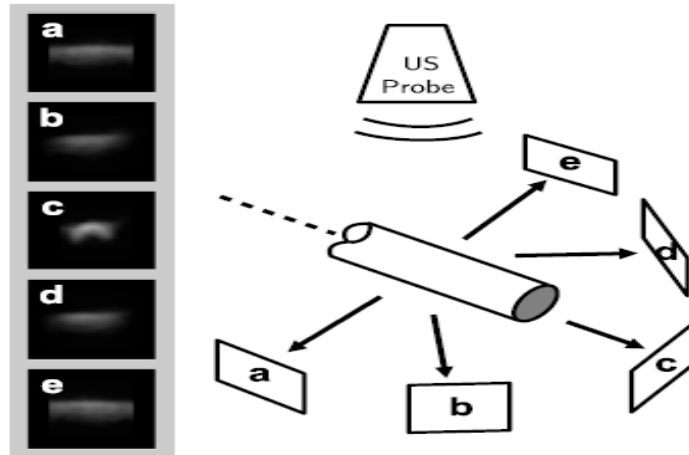


Figure 3.1 Example of Radon Transform: Image (a–e) is a projection of the ultrasound image along the corresponding direction shown in the schematic. The projection along the axis of the instrument (c) is the brightest [20].

To detect the tip location, the authors use a new marker design shown in figure 3.2. Bumps are identified using template matching on ultrasound slice. The positions of the three best matches found in the slice are used to determine the tip position of the instrument and the roll angle.

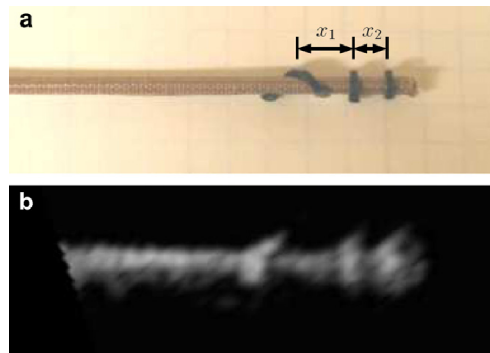


Figure 3.2 (a) Picture (b) ultrasound image of the needle with passive markers [20].

Initially, equation 3.12 is calculated for evenly spaced points throughout the volume space I . The volume is sampled at 5 voxel increments in x , y , and z . For angles Φ , θ , equation 3.12 is sampled in 10 degrees increments from 0 to 180 degrees. In this way, the initial coordinates of

the instrument are found. For subsequent frames, the tracking algorithm confines its search space to an area centered on the location found in the previous frame.

Results show this implementation detected a surgical instrument in 31 ms, sufficient for real-time tracking at the 25 volumes per second rate of the ultrasound machine. A water tank experiment found instrument orientation errors of 1.1 degree and tip position errors of less than 1.8 mm.

3.3.1 Shortcomings of Radon transform approach

This work uses passive markers to detect the needle tip. This requires wrapping of 800 μm polyurethane foam around the instrument shaft (figure 3.2). Polyurethane can cause allergic reactions to eyes, nose, throat, lungs and skin [49]. Even with the markers, the algorithm sometimes incorrectly identifies the position of the passive markers.

This method is also computationally exhaustive. It requires five parallel graphical processing units to calculate the five parameters x , y , z , Φ and θ discussed above. Also, sixteen parallel programs are needed to be executed using the graphic card to calculate the integral in equation 3.12.

3.4 Parallel Integral Projection

The PIP is a transform that maps an image function $I : \mathbb{R}^3 \rightarrow \mathbb{R}$ representing volume data to a function $PI : \mathbb{R}^4 \rightarrow \mathbb{R}$ [22] describing its projections (see figure 3.3) as a function of the 2-D displacement (u, v) and the projection direction determined by two angles (α, β)

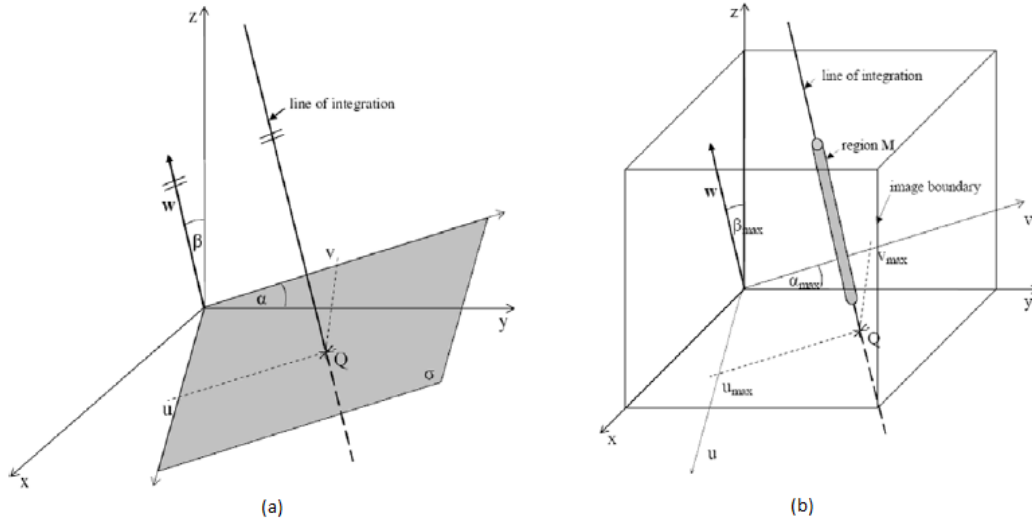


Figure 3.3 (a) Integral of the image intensity function is calculated along a line given by the point $Q [u, v]$ and a vector w . (b) Evaluation of the PIP transformation of a 3-D image [22]

So PIP is defined as:

$$P(\alpha, \beta, u, v) = \int_{-\infty}^{\infty} I(R(\alpha, \beta) \cdot (u, v, t)^T) dt \quad (3.13)$$

Where $R(\alpha, \beta)$ is a rotational matrix given by:

$$R(\alpha, \beta) = \begin{pmatrix} \cos\beta & \sin\alpha * \sin\beta & -\cos\alpha * \sin\beta \\ 0 & \cos\alpha & \sin\alpha \\ \sin\beta & -\sin\alpha * \cos\beta & \cos\alpha * \cos\beta \end{pmatrix} \quad (3.14)$$

The axis of electrode is identified in 3D image using the following steps:

Let $I: R^3 \rightarrow R$ be an image function such that intensity of the electrode M is greater than the background:

$$\forall x_1 \in M, \forall x_2 \notin M, I(x_1) > I(x_2) \quad (3.15)$$

When the electrode diameter is infinitely small, PIP transform $P(\alpha, \beta, u, v)$ has the maximum when the line of integration is coincident with the axis of M :

$$(u_{max}, v_{max}, \alpha_{max}, \beta_{max}) = \operatorname{argmax} P(u, v, \alpha, \beta)$$

Discretization of the PIP Transformation: The authors maximize PIP transform on a discrete grid such that the discretization steps Δ_α , Δ_β , Δ_u , Δ_v are sufficiently fine not to miss the electrode.

That is,

$$\Delta_\alpha, \Delta_\beta \leq 2 \arctan \frac{d}{2 * \|x_{max}\|} \quad (3.16)$$

$$\Delta_u, \Delta_v \leq d, \quad (3.17)$$

where, d is the electrode diameter and x_{max} is the position of the most distant voxel from the origin.

Maximizing the PIP Transformation: The authors decompose the maximization of $PI(u, v, \alpha, \beta)$ to an inner maximization with respect to (u, v) and an outer maximization with respect to (α, β) .

$A(\alpha, \beta)$ is angle function which is maximized by α_{max} , β_{max} and maximizes $P(u, v, \alpha, \beta)$ for u_{max} ,

v_{max} :

$$A(\alpha, \beta) = \max_{u, v} P(u, v, \alpha, \beta) \quad (3.18)$$

They then use a hierarchical mesh-grid search (figure 3.4) to find maximum of $A(\alpha, \beta)$ [23].

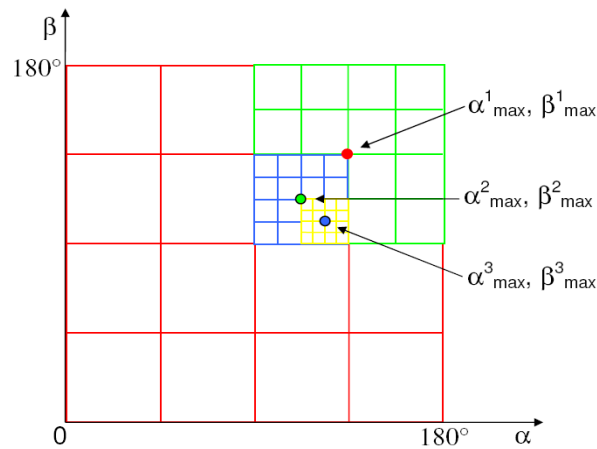


Figure 3.4 Principle of hierarchical mesh-grid algorithm [22]

On the first level, $A(\alpha, \beta)$ is evaluated on a rectangular grid of points $\langle 0^\circ, 180^\circ \rangle \times \langle 0^\circ, 180^\circ \rangle$ that are uniformly sampled with steps $\Delta_{\alpha}^{\text{init}}, \Delta_{\beta}^{\text{init}}$. The maximum location $(\alpha_{\text{max}}^1, \beta_{\text{max}}^1)$ is determined. On the second level, the angle function is evaluated on a rectangular grid $\langle \alpha_{\text{max}}^1 - 45^\circ, \alpha_{\text{max}}^1 + 45^\circ \rangle \times \langle \beta_{\text{max}}^1 - 45^\circ, \beta_{\text{max}}^1 + 45^\circ \rangle$ uniformly sampled with steps $\Delta_{\alpha}^2 = (\Delta_{\alpha}^1/2), \Delta_{\beta}^2 = (\Delta_{\beta}^1/2)$, where $\Delta_{\alpha}^1 = \Delta_{\alpha}^{\text{init}}, \Delta_{\beta}^1 = \Delta_{\beta}^{\text{init}}$. The pair $(\alpha_{\text{max}}^2, \beta_{\text{max}}^2)$ that maximizes $A(\alpha, \beta)$ is established. This algorithm is repeated for i levels until both steps $\Delta_{\alpha}^i, \Delta_{\beta}^i$ are equal, figure 3.4.

Results show experiments were performed on numerical phantoms with localization accuracy between 0.2 and 0.3 mm for real images. But processing time for current MATLAB implementation is tens of minutes.

3.4.1 Shortcomings of Parallel Integral Projection

This approach is not feasible for real time applications due to its processing speed. The processing time of the current algorithm implementation in MATLAB is tens of minutes. Even rewriting the method in a compiled language such as C or Java will likely not allow real time implementation.

This algorithm makes two assumptions: electrode appears as a cylindrical object with a straight axis and, the intensity of electrode voxels is much higher than the intensity of background voxels. So, in an in vivo situation, where above assumptions are not true, this algorithm will not accurately segment the needle.

3.5 Model fitting using RANSAC

Martin Barva [1, 24, 25] proposed an algorithm for finding needle axis and tip using model fitting using RANSAC. Given input data set model and a cost function, RANSAC provides, with a certain predetermined probability, the model parameters that maximize the cost function and all inliers consistent with the corresponding model. The algorithm is based on the following two assumptions.

1. *Assumption 1:* The intensity of the tool's voxels is higher than the surrounding tissue.

2. *Assumption 2:* The shape of the tool is a thin, long, and possibly curved cylinder.

The propose algorithm consists of following steps:

3.5.1 Thresholding

A set of voxels with coordinates $X \subseteq \mathbb{R}^3$ and intensities $I(X) \subseteq \mathbb{R}$ is split by thresholding (using Assumption 1) into two disjoint sets: X_t (tool's voxels) and X_b (background voxels)

$$X_t = \{x \in X: I(x) \geq T_t\} \quad X = X \setminus X_t \quad (3.19)$$

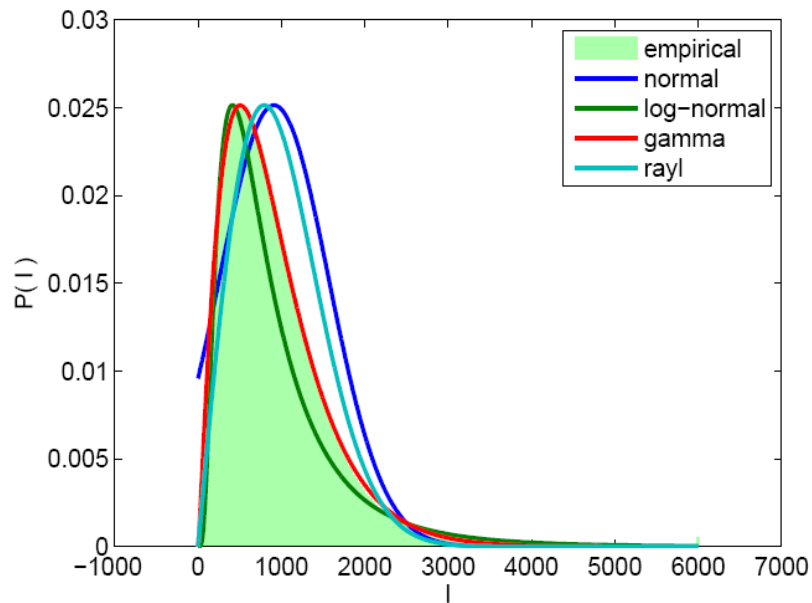


Figure 3.5 Statistical models of the intensity distribution. The parameters of four probability distributions were estimated to fit the intensity of training images [1].

Barva estimates the threshold T_t as the 95% quartile of the input data by fitting Gamma distribution [24]. This is based on the expectation that the proportion of voxels belonging to the tool is less than 5%.

3.5.2 Axis localization

The tool's axis is represented by a spatial parametric polynomial curve $c(t;H): \mathbb{R} \rightarrow \mathbb{R}^3$ of order $n - 1$

$$c(t;H) = \begin{pmatrix} h_{11} & h_{12} & h_{13} & h_{14} \\ h_{21} & h_{22} & h_{23} & h_{24} \\ h_{31} & h_{32} & h_{33} & h_{34} \\ h_{41} & h_{42} & h_{43} & h_{44} \end{pmatrix} \cdot \begin{pmatrix} 1 \\ t \\ t^2 \\ t^3 \end{pmatrix}; t \in \mathbb{R} \quad (3.20)$$

Where H is a matrix of curve coefficients and t is a curve parameter. They defined a cubic curve (figure 3.6) by means of four points (denoted as the control points) that lie on the curve.

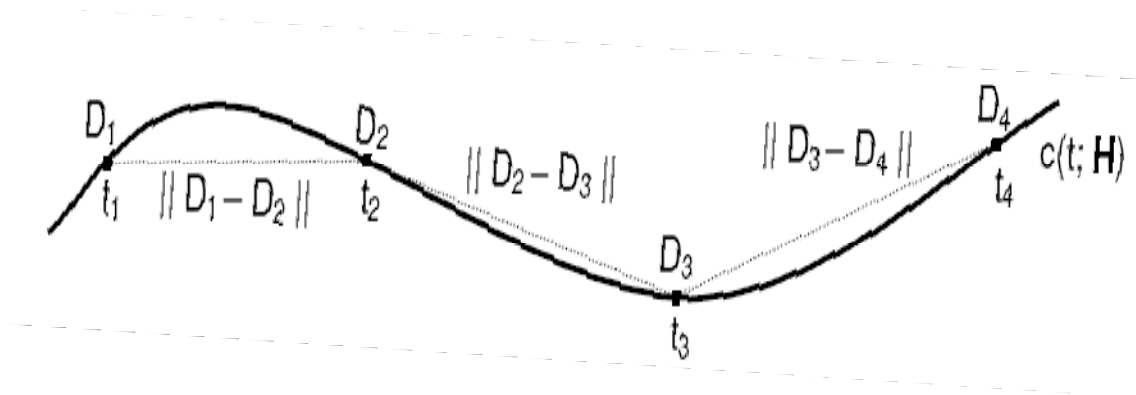


Figure 3.6 Parametric cubical curve [1].

They deduced an H matrix using $D = (D_1, D_2, D_3, D_4)$. The curve parameters t_1, t_2, t_3, t_4 of the control points, which are required to determine H , are not known a priori. They let $t_1 = 0$. And deduce the values of the other curve parameters t_2, t_3, t_4 from Euclidean distances between adjacent control points to approximate the true arc length parameters:

$$t_2 = \|D_1 - D_2\| \quad (3.21)$$

$$t_3 = t_2 + \|D_2 - D_3\| \quad (3.22)$$

$$t_4 = t_3 + \|D_3 - D_4\| \quad (3.23)$$

So condition imposed on H is:

$$\begin{pmatrix} h_{11} & h_{12} & h_{13} & h_{14} \\ h_{21} & h_{22} & h_{23} & h_{24} \\ h_{31} & h_{32} & h_{33} & h_{34} \\ h_{41} & h_{42} & h_{43} & h_{44} \end{pmatrix} \cdot \begin{pmatrix} 1 & 1 & 1 & 1 \\ t_1 & t_2 & t_3 & t_4 \\ t_1^2 & t_2^2 & t_3^2 & t_4^2 \\ t_1^3 & t_2^3 & t_3^3 & t_4^3 \end{pmatrix} = \begin{pmatrix} D_{1,x} & D_{2,x} & D_{3,x} & D_{4,x} \\ D_{1,y} & D_{2,y} & D_{3,y} & D_{4,y} \\ D_{1,z} & D_{2,z} & D_{3,z} & D_{4,z} \end{pmatrix} \quad (3.24)$$

$$\text{Or, } H = D \cdot T^{-1}$$

3.5.3 Shortcomings of model fitting approach

The optimal value of T_i was deduced from the estimated statistical model that describes the voxel intensities (figure 3.5). The model parameters were estimated using a training set of five ultrasound images acquired by scanning a portion of tissue containing an electrode. But, in real time biopsies, it will not be always possible to establish prior intensity distributions.

Like the parallel integral projection approach, two assumptions were made: the electrode appears as a cylindrical object with a straight axis and, the intensity of electrode voxels is much higher than the intensity of background voxels. Then using thresholding, image intensities are split into two disjoint sets: X_t (tool's voxels) and X_b (background voxels). So, this approach will likely fail to the isolate tool's voxels for real ultrasound images.

Table 3.2 summarizes the methods discussed above. Also it compares the angle accuracy, positional accuracy and computational time for them.

Table 3.2 Comparison of previous work: Object localization and segmentation.

Method	Basic Idea	Angle accuracy	Length accuracy	Computational Time
3DHT	Uses extension of 2D Hough Transform. New representation of line in 3D is discussed. Requires a priori knowledge of needle position and orientation.	1.30 ⁰	1.76 mm	3.03 s (Visual C++)
3DRHT	Concept is same as 3DHT but different implementation is used. Instead of linearly sampling, this iteratively samples random points in thresholded image and increments corresponding bins in the accumulator.	2.62 ⁰	2.39 mm	0.10 s (Visual C++)
Radon Transform	Radon transform is the integral transform consisting of the integral of a function over straight lines. Lines are identified as the local maximums of the integration results.	1.1 ⁰	1.88 mm	31 ms (used parallel processing and GPU)
Parallel integral projection (PIP)	PIP transforms maps the 3D image to its 2D projections in terms of the 2-D displacement (u , v) and the projection direction determined by two angles (α , β). The PIP transform is similar to the Radon transform.	Not Available	0.2 -0.3 mm	10 -20 minutes (MATLAB)
Principal Component Analysis (PCA)	PCA uses an orthogonal transformation to convert a set of observations of possibly correlated variables into a set of uncorrelated variables called principal components, thereby decreasing the number of components required to represent the data.	Less than 4 ⁰	1mm	Not Available

*All data is taken from the corresponding articles and different data sets were used for experiments.

The Radon transform approach gives the best accuracy for angular deviation but, at the cost of computational time and the hardware required (table 3.2). We get the best accuracy for tool length deviation by PIP approach but like Radon Transform, this approach is not efficient for real time applications. The PCA approach gives good results both in terms of accuracy and computational cost if the needle is the only structure in the image.

Work in this thesis uses images which are likely to be much closer to the images encountered in in-vivo situations. We consulted two practicing interventional radiologists, Dr. Katherine Holly at the Baylor Hospital, Dallas, TX and Dr. Robert Wynn at UT Southwestern Medical Center. In addition Dr. Mathew Lewis, a cancer researcher at UT Southwestern Medical Center also gave us substantial advice on procuring realistic US images obtained using realistic phantoms. Thus our US images are distorted due to the presence of artifacts and speckle noise. The contrast between the intensity of the needle and the background is not high. Also needle boundaries are distorted and they do not appear as perfect straight lines in the images. So, we cannot use PCA, model fitting using RANSAC or PIP approach. Between Radon transform and Hough transform, the latter is better in terms of the computational and underlying hardware cost requirement.

But image enhancement is required due to degraded images used in this work. Image enhancement using diffusion filters is described in chapter 4.

CHAPTER 4

DIFFUSION FILTERS FOR SPECKLE RESUCTION

Ultrasound images suffer from speckle due to the interference of back-scattered signal [28]. It is caused by the interference of energy from randomly distributed scatters, which is too small to be resolved by the imaging system. The speckle noise is the limiting factor for image contrast in US images and produces the familiar apparently random modulation of the image in regions that would otherwise be displayed as a uniform gray level, so the speckle significantly degrades the image quality and hinders the discrimination of the fine details [29].

Image filtering is one of the steps used in image processing to remove the noise. The traditional methods of de-noising, using simple filters as a Gaussian filter not only smooth the noise in the image but also, blur the edges and change their location. Alternative methods based on partial differential equation [26, 28] have been proposed to address this problem.

4.1 Speckle Model

Speckle pattern can be categorized into one of the following three classes according to the number of scatters per resolution cell also known as scatter number density.(SND) [27].

Fully Formed Speckle pattern - This occurs when many randomly distributed scattering sites exist within the resolution cell $SND > 10$. The amplitude of the backscattered signal can be modeled as a Rayleigh distributed random variable [27, 29].

Nonrandomly distributed with long-range order [30] - This occur due to the correlation between scatterers, and hence the effective number of scatterers is finite $SND < 10$. This case is modeled by the K-distribution [29].

Nonrandomly distributed with short-range order [30] - This occurs when a spatially invariant coherent structure is present within the random scatterer region [27]. The probability density function (PDF) of the backscattered signals becomes close to the Rician distribution [29].

Hence, the coherence phenomena make the SNR an ambiguous feature that cannot be used alone to characterize the speckle model.

4.2 Diffusion Filters

4.2.1 Physical background of diffusion filters

Diffusion is a physical process that equilibrates concentration differences without creating or destroying mass [28]. The equilibration property is expressed by Fick's law that relates the diffusive flux 'j' to the concentration gradient ∇u , by postulating that the flux goes from regions of high concentration to regions of low concentration, with a magnitude that is proportional to the concentration gradient :

$$j = -D \cdot \nabla u \quad (4.1)$$

where, D is the diffusion tensor, a positive definite symmetric matrix.

The case when j and ∇u are parallel is called isotropic and we may replace the diffusion tensor by a positive scalar-valued diffusivity g. Continuity equation, i.e., the statement that the rate at which mass enters a system is equal to the rate at which mass leaves the system, can be expressed by

$$\partial_t u = -\text{div } j \quad (4.2)$$

If we combine equation 4.1 and equation 4.2 we get diffusion equation:

$$\partial_t u = -\text{div } (D \cdot \nabla u) \quad (4.3)$$

If the diffusion tensor D is constant over the whole image domain, then equation 4.3 represents homogeneous diffusion. A space-dependent filtering is called inhomogeneous diffusion [28]. Often the diffusion tensor is a function of the differential structure of the evolving image itself. Then above equation represents nonlinear diffusion filters. Diffusion which does not depend on the evolving image is called linear.

4.2.2 Linear Diffusion Filters

Linear Homogeneous diffusion process, where image intensity I is being diffused is given by:

$$\frac{\partial I}{\partial t} = \nabla \cdot (c \nabla I) ; \text{At } t=0 \ I(x,y;0) = f(x,y) \quad (4.4)$$

where, diffusion coefficient c has a constant value and ∇ . and ∇ are divergence and gradient operators respectively [33]. Linear diffusion filtering is equivalent to convolution with a Gaussian which is given by:

$$g(x, y, t) = \frac{1}{2\pi t^2} e^{-(x^2 + y^2)/2t^2} \quad (4.5)$$

$$L(x,y;t) = g(x,y,t) * f(x,y) ; \text{at } t = 0 \ L(x,y,0) = f(x,y)$$

Linear diffusion filters are used for multi-scale segmentation of the image. As t increases, $I(x,y,t)$ is the result of smoothing f with a larger and larger filter, thereby removing more and more of the details in the image. The idea is to identify segments at coarse scales and to link backwards to the original image in order to improve localization [28].

Limitations of linear diffusion filtering:

It does not only smooth noise, but also blurs important features such as edges and, thus, makes them harder to identify.

Linear diffusion filtering dislocates edges when moving from finer to coarser scales [34]. So structures which are identified at a coarse scale do not give the right location and have to be traced back to the original image.

4.2.3 Nonlinear Diffusion Filter

4.2.3.1 The Perona–Malik model (Nonlinear isotropic diffusion models) [26]

Perona and Malik introduced a nonlinear isotropic diffusion method, which avoids the blurring and localization problems of linear diffusion filtering described in section 4.2.2, by applying an inhomogeneous process that reduces the diffusivity at those locations, which have larger likelihood to be edges. The likelihood of edges is proportional to $|\nabla u|^2$:

$$\partial_t u = \text{div}(g(|\nabla u|^2) \nabla u) \quad (4.6)$$

where, diffusivity $g(\cdot)$ is given by:

$$g(|\nabla u|^2) = \frac{1}{(1 + \frac{|\nabla u|^2}{\lambda^2})} \quad (4.7)$$

or,

$$g(|\nabla u|^2) = \exp\left(-\left(\frac{|\nabla u|}{\lambda}\right)^2\right) \quad (4.8)$$

For the diffusivity (equation 4.7) it follows that the flux function $\theta(s) := sg(s^2)$ satisfies $\theta'(s) \geq 0$ for $|s| \leq \lambda$, and $\theta'(s) < 0$ for $|s| > \lambda$.

Canny edge detector is based on calculating the first derivatives of the Gaussian-smoothed image. After applying sophisticated thinning and linking mechanisms (non-maxima suppression and hysteresis thresholding), edges are identified as locations where the gradient magnitude has a maximum. This method is often acknowledged to be the best linear edge detector, and it has become a standard in edge detection.

The experiments of Perona and Malik demonstrated that edge detection based on this process gave better results compared to the linear Canny edge detector, even without applying non-maxima suppression and hysteresis thresholding.

4.2.3.2 Regularized Perona–Malik model

To overcome theoretical instabilities of Perona–Malik [28] some numerical schemes were introduced. The first spatial regularization attempt is due to Posmentier, who observed numerically, the stabilizing effect of averaging the gradient within the diffusivity [35, 28]. Mathematical formulation of this idea is done by [36], replacing the diffusivity $g(|\nabla u|^2)$ of the Perona–Malik model by a Gaussian-smoothed version $g(|\nabla u_\sigma|^2)$ with $u_\sigma := K_\sigma * u$, where K_σ is a Gaussian filter given by:

$$K_\sigma(x, y) = \frac{1}{2\pi\sigma^2} \exp\left(-\frac{|x|^2 + |y|^2}{2\sigma^2}\right) \quad (4.09)$$

And thus, diffusion filter is given by:

$$\partial_t u = \text{div}(g(|\nabla u_\sigma|^2)\nabla u) \quad (4.10)$$

4.2.3.3 Nonlinear anisotropic diffusion models

The Perona–Malik model and its regularized form used scalar-valued diffusivity g , which is adapted to the likelihood of edges. Therefore, the flux $j = -g\nabla u$ is always parallel to ∇u . But, for the edge detection, it is desirable to bias the flux towards the orientation of edges. To fulfill these requirements, a diffusion tensor leading to anisotropic diffusion filters was introduced.

4.2.3.4 Anisotropic regularization of the Perona–Malik model for edge enhancement

The non-homogeneous isotropic diffusion limits the smoothing of an image near pixels with a large gradient magnitude, which are essentially the edge pixels. As the diffusion near an edge is minimal, the noise reduction near the edge is also small. To address this, anisotropic diffusion was proposed to allow the diffusion to be different along different directions. For Anisotropic models, we have to consider the direction of the edge detector ∇u_σ also, along with the magnitude $|\nabla u_\sigma|$. For edge detection, the orthonormal system of eigenvectors v_1, v_2 of diffusion tensor was adapted [37]:

$$v_1 \parallel \nabla u_\sigma ; v_2 \perp \nabla u_\sigma \quad (4.11)$$

In order to perform smoothing along the edge and not across it, Weickert [38] proposed to choose the corresponding eigenvalues λ_1 and λ_2 as:

$$\lambda_1(\nabla u_\sigma) = g(|\nabla u_\sigma|^2) ; \lambda_2(\nabla u_\sigma) = 1 \quad (4.12)$$

$$\text{and } g(s) = \begin{cases} 1 & \text{for } s \leq 0 \\ 1 - \exp\left(-\frac{c_m}{\left(\frac{s}{\lambda}\right)^m}\right) & \text{for } s > 0 \end{cases} , \quad (4.13)$$

$$1 = \exp(-Cm)(1 + 2Cmm). \quad (4.14)$$

The constant C_m is calculated in such a way that the flux $\theta(s) := sg(s)$ is increasing for $s \in [0, \lambda]$ and decreasing for $s \in (\lambda, \infty)$. Thus, it is regarded as an anisotropic regularization of the Perona–Malik model [28].

In this thesis work, edge enhancing nonlinear anisotropic diffusion filter was used (equation 4.10 and 4.13), as nonlinear diffusion avoids blurring at those locations, which have larger likelihood to be edges. Results of actual simulation to demonstrate the difference between linear and nonlinear anisotropic diffusion are shown in chapter 5, section 5.2.

CHAPTER 5

ALGORITHM FOR NEEDLE SEGMENTATION AND SIMULATIONS

In most of the previous work described in chapter 3, the authors assumed the needle to be brighter than the background. None of these approaches applied any image enhancement algorithms to remove the speckle noise or other artifacts. They just focused on using different forms of edge detection algorithms (Hough transform approach, Radon transform, principal component analysis or parallel integral projection approach) to find the needle location.

But this assumption, that the needle is brighter than the background, is not always true. The needle is brightest in the case when ultrasound transducer is perpendicular to the needle axis. But as the angle between transducer and the needle axis starts decreasing from 90° , needle becomes less bright. There are other artifacts like reverberation, which occurs when ultrasound is repeatedly reflected between two highly reflective surfaces, resulting in an identical artifactual image. Also, ultrasound images suffer from speckle noise, which significantly degrades the image quality and causes distortion at needle boundaries, as described in chapter 4. Figure 5.1 shows the comparison of the data used by some of the aforementioned work and this thesis.

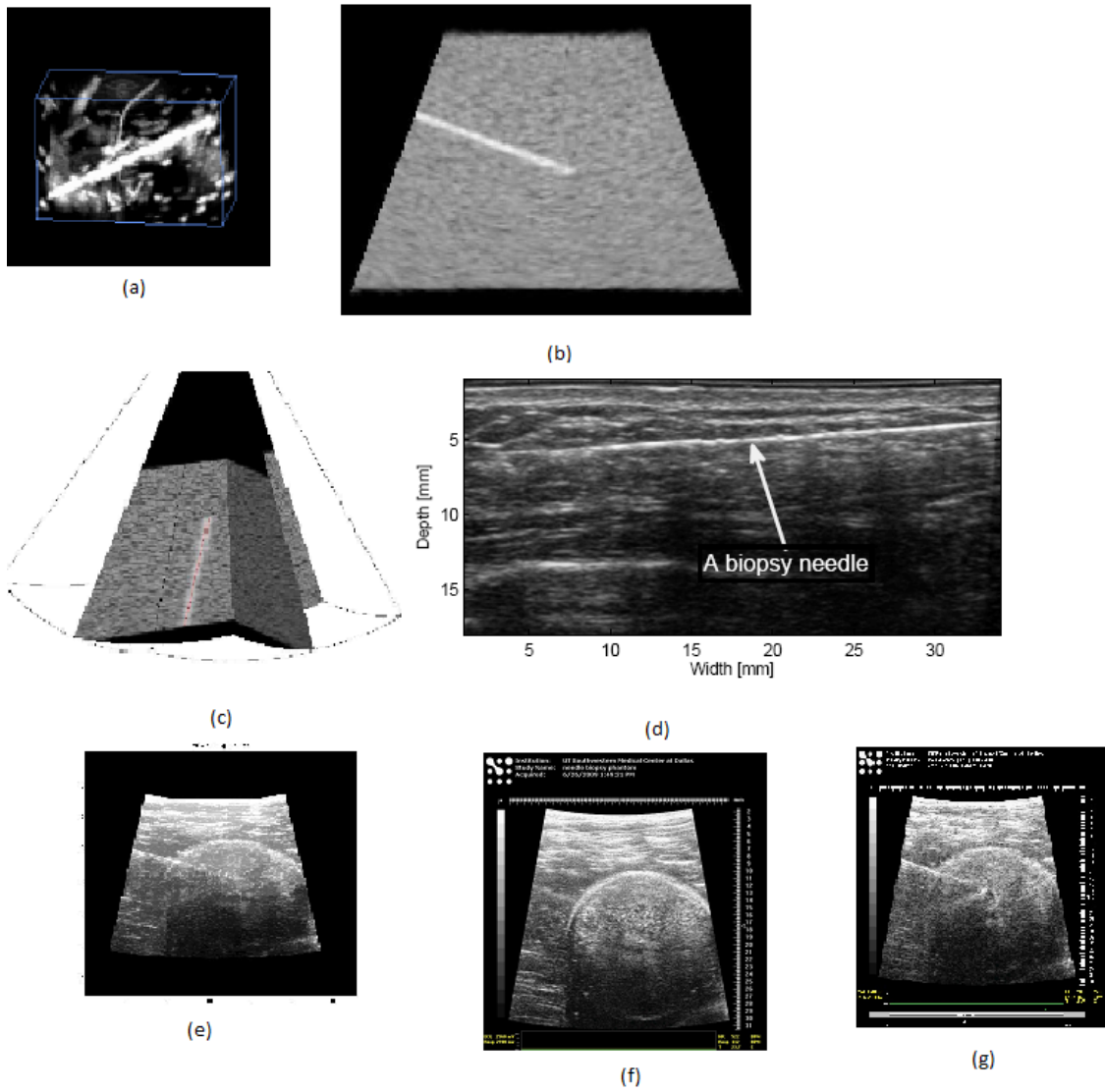


Figure 5.1 Comparison of data set used by some of the researches (a) used in article [10] (b) used in article [8] (c) used in article [1] (d) used in article [22] (e), (f), (g) used in this work

In this thesis, cases in which the needle is not brighter than the background due to reverberation artifacts (figure 5.1 (g)) and speckle noise (figure 5.1 (f)) are also considered.

Considering the presence of speckle and artifacts in the data used for this thesis, various approaches to enhance the ultrasound images by removing the speckle without destroying important image features, like needle in this case were reviewed [27, 29, 50, 51, 52, 53]. Extensive work is done in the field of enhancing images using partial differential equation based diffusion filters. There are also articles related to edge enhancing diffusion filters. Results established in previous works indicated the effectiveness of diffusion filters in the problems related to edge enhancement and speckle reduction. Approaches to improve the feature boundaries were also analyzed, to reduce the distortion in the needle boundaries and hence improve the chances of segmentation. Finally, work related to edge detection and feature segmentation were studied. Some of the work in this field addressed the issue of segmenting surgical tools in ultrasound images, but by neglecting the presence of speckle and other artifacts in the considered data.

Figure 5.2 shows the accurate needle detection in speckled US images algorithm (ANDSUI) used in this thesis work. In the ANDSUI algorithm, ultrasound images are first enhanced using a nonlinear diffusion filter, staggered components are removed using connected component analysis, needle boundaries are improved using morphological closing and 2nd order Gaussian filter is used and finally the needle is segmented using gray scale Hough transform.

Following sections discuss each step of the algorithm and results by applying these steps on ultrasound images in detail.

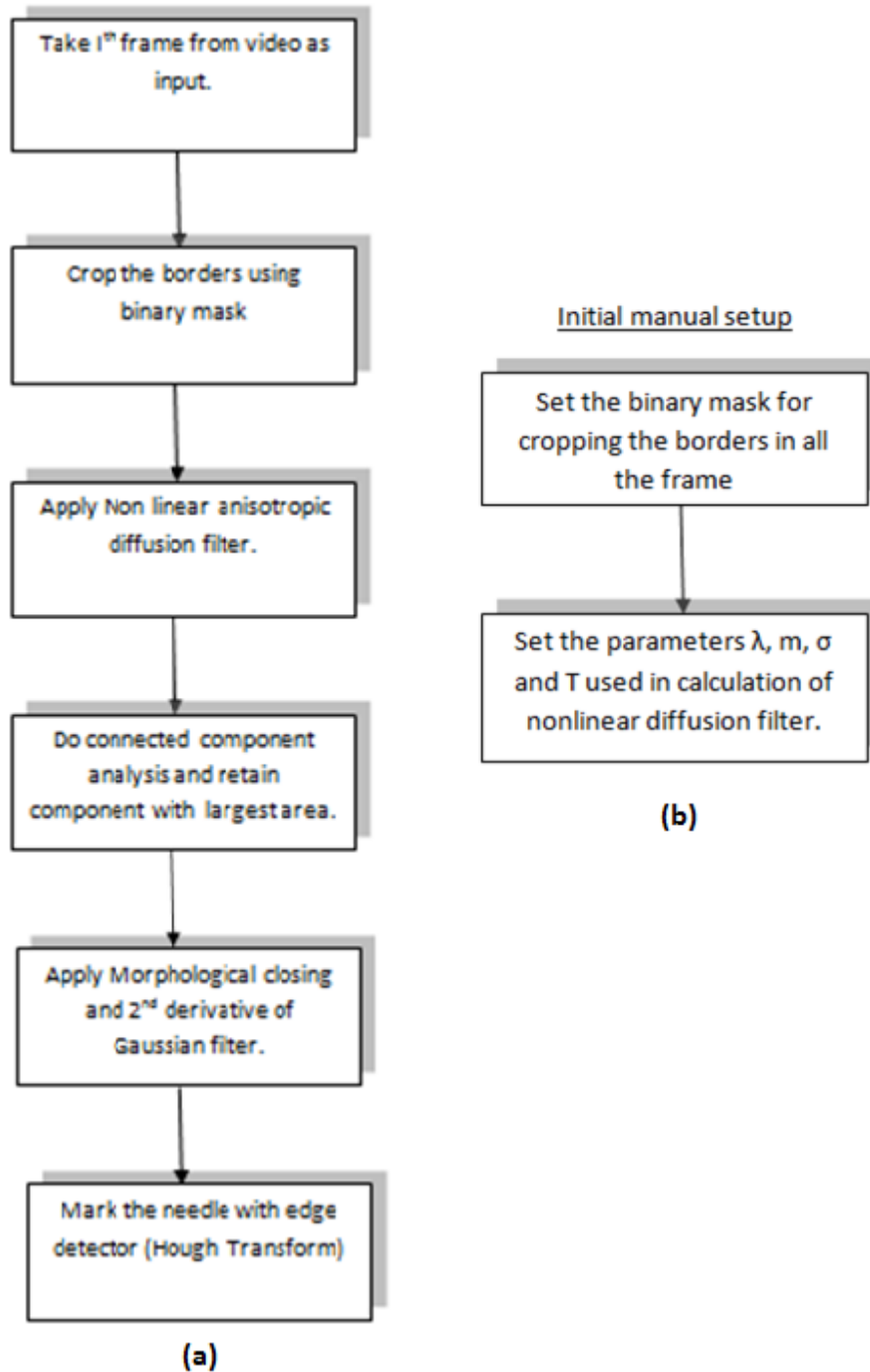


Figure 5.2 Flowchart for the Accurate Needle Detection in Speckled US Images algorithm (a) Steps in ANDSUI algorithm (b) Initial manual settings.

5.1 Cropping borders

The first step after choosing the input frame is to remove the unwanted borders. Although this might seem like a simple, even primitive step and reasonably obvious at first glance, it turned out to have far reaching implications for this class of practical US images commonly used today. It neatly avoids false results when future steps are applied. Borders are cropped by creating a binary mask (Fig 5.3 (b)). This binary mask is inverted and then applied to the original image to obtain the cropped image (Fig 5.3).

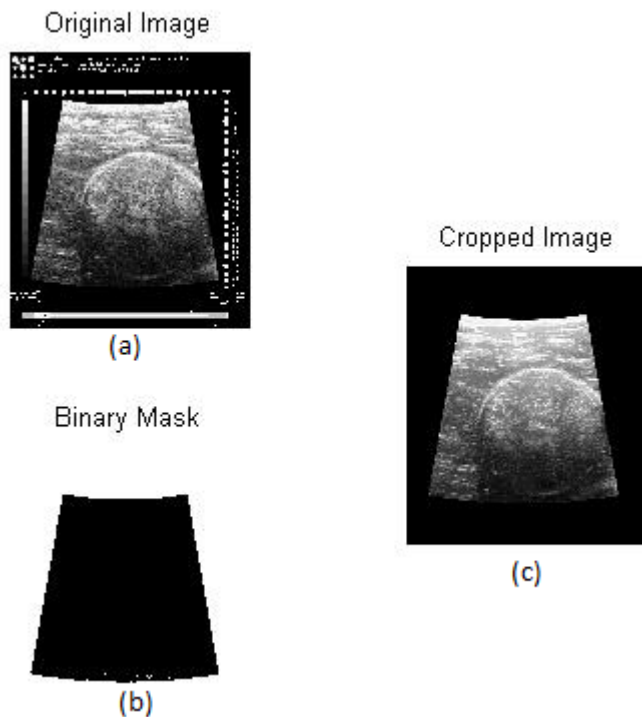


Figure 5.3(a) Original image (b) Binary mask (c) Cropped image after removal of the borders.

5.2 Nonlinear anisotropic diffusion filter

Ultrasound images suffer from speckle noise. Diffusion filters based on the partial differential equation are used to enhance the image quality.

5.2.1 Demonstration of difference between linear and nonlinear anisotropic diffusion.

Figure 5.4 demonstrate the difference in output when linear and non linear anisotropic diffusion filters are applied to the same simulated image. So, linear diffusion does not only smooth noise, but also blurs important features such as edges and, thus, makes them harder to identify. But, nonlinear diffusion avoids blurring by applying an inhomogeneous process that reduces the diffusivity at those locations which have larger likelihood to be edges.

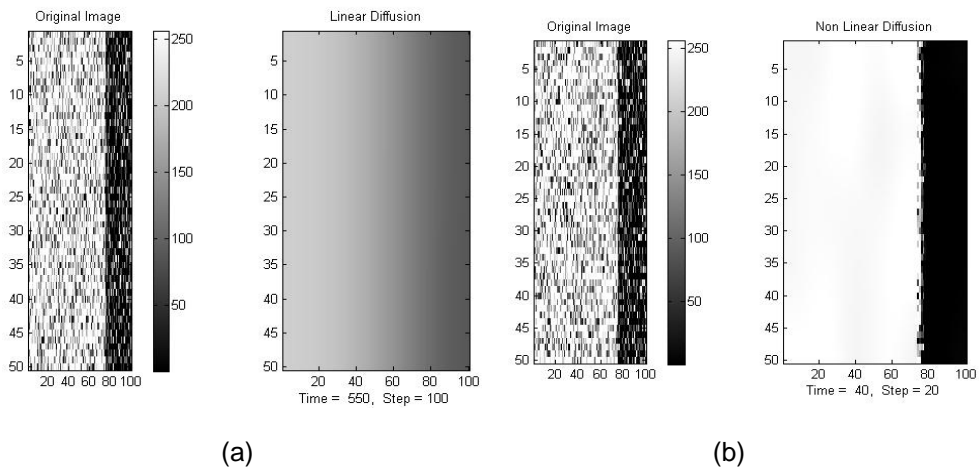


Figure 5.4 Demo to show the difference between linear and nonlinear diffusion.(a) Linear Diffusion(b) Nonlinear diffusion.

5.2.2 Effect of Parameters used in the calculations for nonlinear diffusion.

There are four parameters which are involved in the calculation of diffusion filters: contrast parameter λ , speed of diffusivity m , space regularization parameter or standard deviation of the Gaussian kernel σ and number of steps T .

5.2.2.1 Contrast parameter λ

Contrast parameter λ is used in the calculation of diffusivity (equation 4.13). As described in section 4.2.3, when gradient is smaller than λ , flux ($\theta(s) := sg(s)$) increases with the gradient (forward) and when gradient is larger than λ , flux decreases as the gradient increase (backward). Also diffusivity decreases monotonically as gradient increases (figure 5.4).

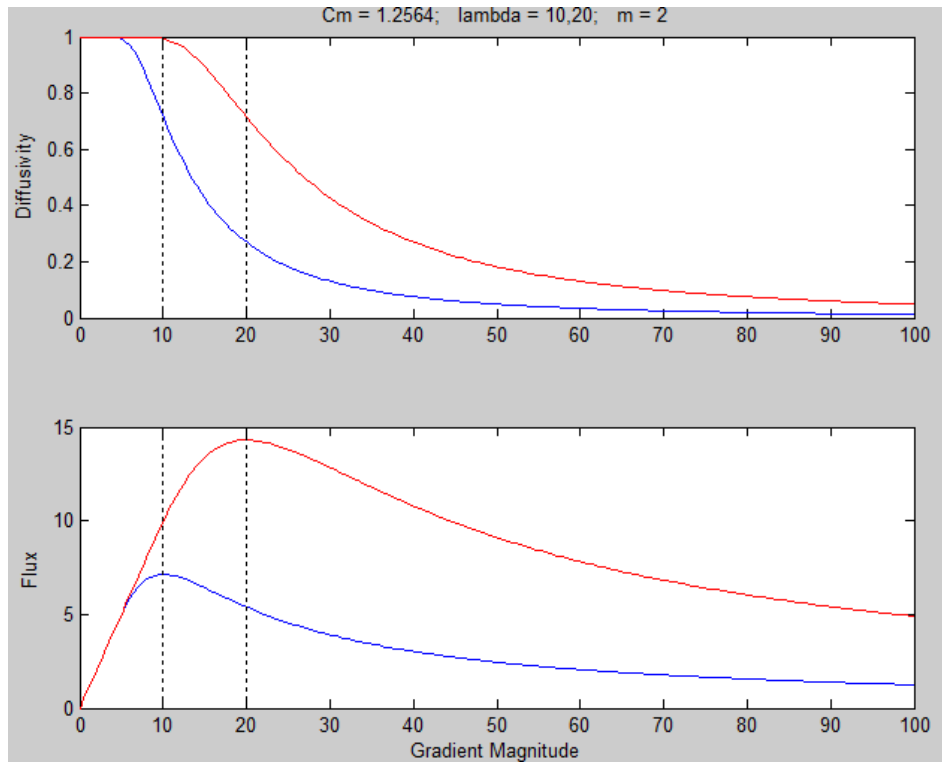


Figure 5.5 Comparison of Diffusivity and Flux with increasing gradient magnitude for $\lambda=10$ (red line) and $\lambda=20$ (blue line).

Hence, λ plays the role of a contrast parameter separating forward (low contrast) from backward (high contrast) diffusion areas. Also, with the increase in λ , diffusivity increases for the same gradient.

Figure 5.6 demonstrates the effect of nonlinear diffusion due to change in λ on US images. So, as λ increases, diffusivity increases. For large values of λ , edges blur. Best choice of λ for the data set used in this thesis work is $2 < \lambda < 5$.

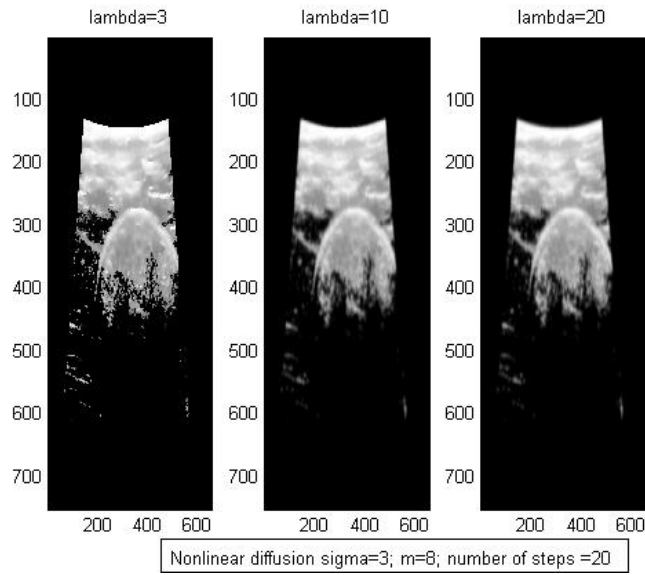


Figure 5.6 Effect of increasing λ on US images. From left to right, λ increase from 3 to 20.

5.2.2.2 Speed of diffusivity m

'm' defines the speed the diffusivity and the flux changes for a variation in the gradient.

Diffusivity and flux changes quickly for larger values of m (figure 5.7).

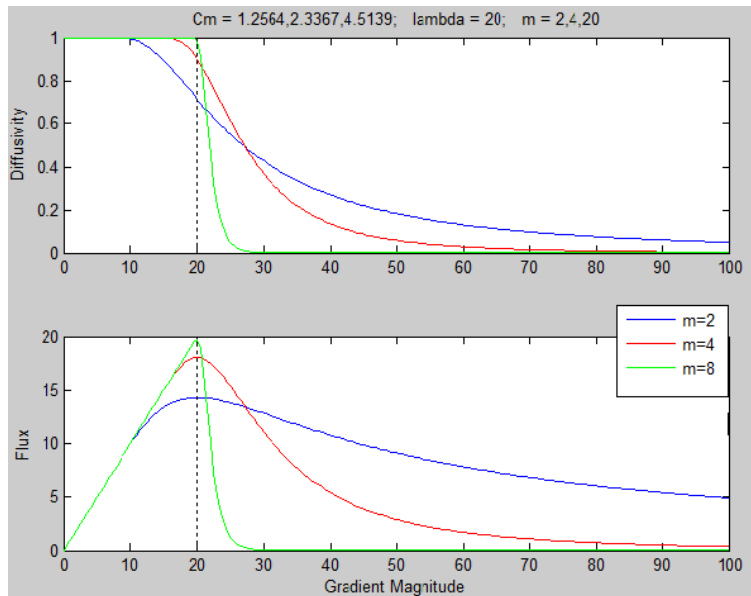


Figure 5.7 Effect of increasing m on Diffusivity and Flux.

A good choice for m is $8 < m < 16$ [28].

5.2.2.3 Space regularization parameter or standard deviation of the Gaussian kernel σ

' σ ' is the standard deviation of the Gaussian filter which is convolved with the image before the gradient is calculated (equation 4.09). The space regularization parameter σ gives the user liberty to adapt nonlinear diffusion scale-spaces to the desired purpose in order to reward interesting features with a longer lifetime [28]. By increasing σ , Gaussian filter becomes faster and more insensitive to small-size structures. But this also leads to stronger blurring of large structures and hence they become difficult to segment (figure 5.8). Best choice of σ for the data set used in this thesis work is $1 < \sigma < 6$.

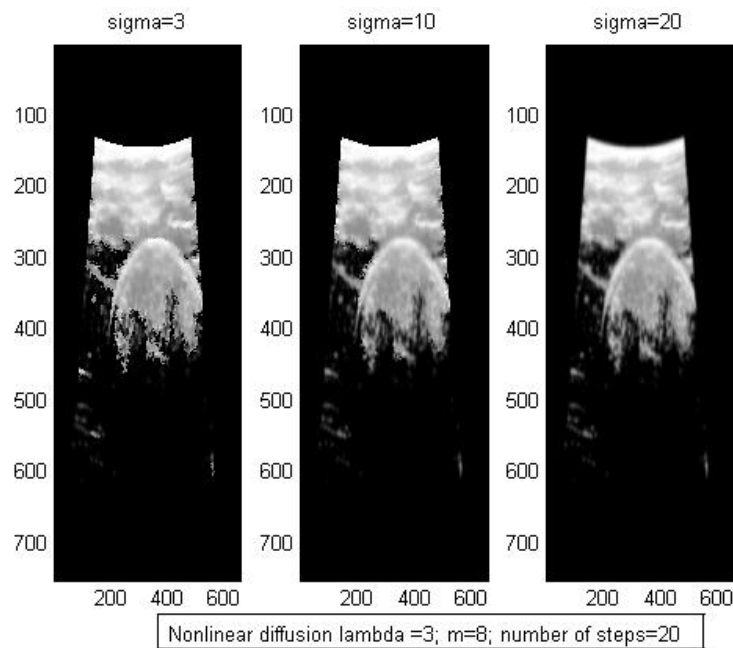


Figure 5.8 Effect of increasing σ on US images. From left to right, σ increase from 3 to 20, keeping λ , m and T fixed.

5.2.2.4 Number of steps T

Number of steps T represents the number of diffusion filter step is repeated. Different values of T provide a family of subsequently simplified versions of the original image, which gives a

hierarchy of structures and allows extracting the relevant information from a certain scale (figure 5.9). Also, by increasing T, execution time for the algorithm increases. Best choice of T for the data set used in this thesis work is $20 < T < 50$.

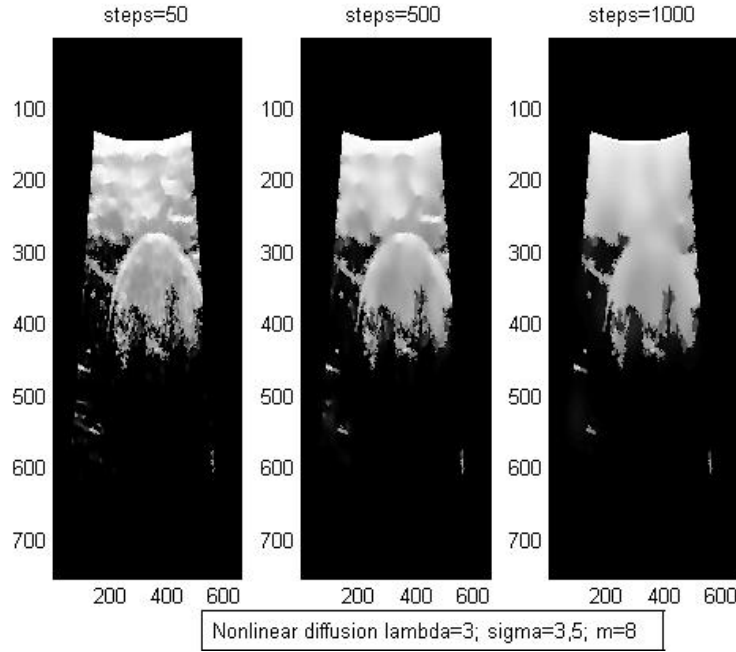


Figure 5.9 Effect of increasing T on US images. From left to right, T increase from 50 to 1000 steps, keeping λ , m and σ fixed.

5.2.3 Simulation results of linear and nonlinear diffusion filter on US images.

Figure 5.10 demonstrates the effect of linear and nonlinear anisotropic diffusion applied on the actual ultrasound image. Linear diffusion filter is implemented using equation 4.4:

$$dy/dt = \text{div}(C \cdot \text{grad}(y)),$$

$$y(0) = u, \quad y(t+T) = y(t) + T \cdot dy/dt, \quad \text{where } T \text{ is the step size.}$$

This process is repeated for the number of steps provided as input by the user. For this experiment, the number of steps is chosen to be 20 and step size as 0.2. 'C' diffusivity constant is taken as 1 for this implementation.

Nonlinear diffusion filter is implemented using equation 4.10:

$$dy/dt = \text{div}(d(\text{grad}(y)).\text{grad}(y)),$$

$$y(0) = u, \quad y(t+T) = y(t) + T \cdot dy/dt, \quad \text{where } T \text{ is the step size.}$$

The diffusivity function (d) is given by the equation 4.13 and constant C_m is calculated using equation 4.14. For this experiment, λ and m (used in calculation of equation 4.13) are taken to be 3 and 8 respectively. Gaussian filter is calculated using equation 4.09 and σ is chosen as 3.5. This process is also repeated for the number of steps input by the user. Again, the number of steps is chosen to be 20 and step size as 0.2.

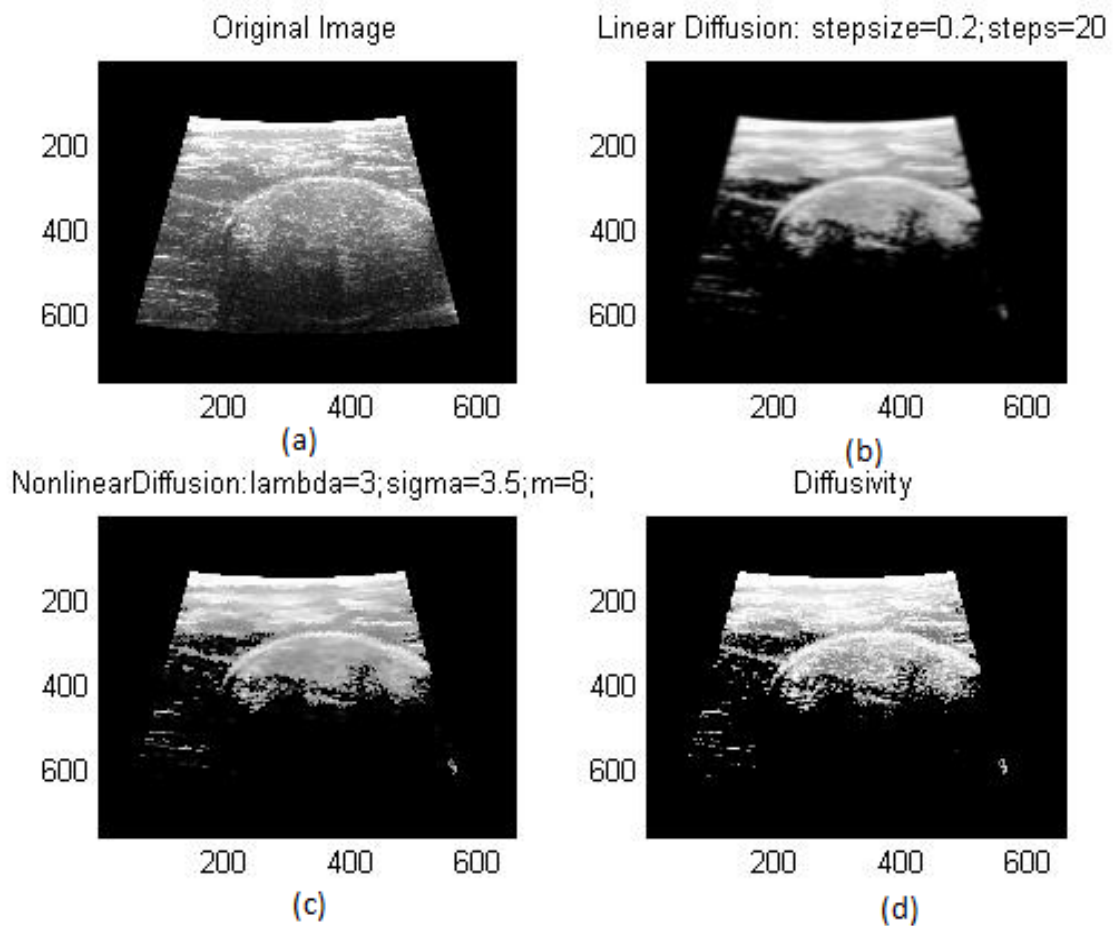


Figure 5.10 Result of Diffusion filter step. (a) Original Image (b) Linear Diffusion (c) Nonlinear Diffusion with (d) Diffusivity used for nonlinear diffusion.

So, for our thesis data, linear diffusion blurs the edges, while nonlinear diffusion maintains the edges and removes the noise. However, it must be pointed out that before the cropping step was performed, even the non-linear diffusion process resulted in a large number of false positives for edges, which would have been mistaken for the needle. Thus, only the combination of the non-linear diffusion and the cropping that eventually resulted in the correct identification of the needle. Clearly this is a case of “human assisted automation”, a seemingly contradictory terminology, but in practice an effective strategy!

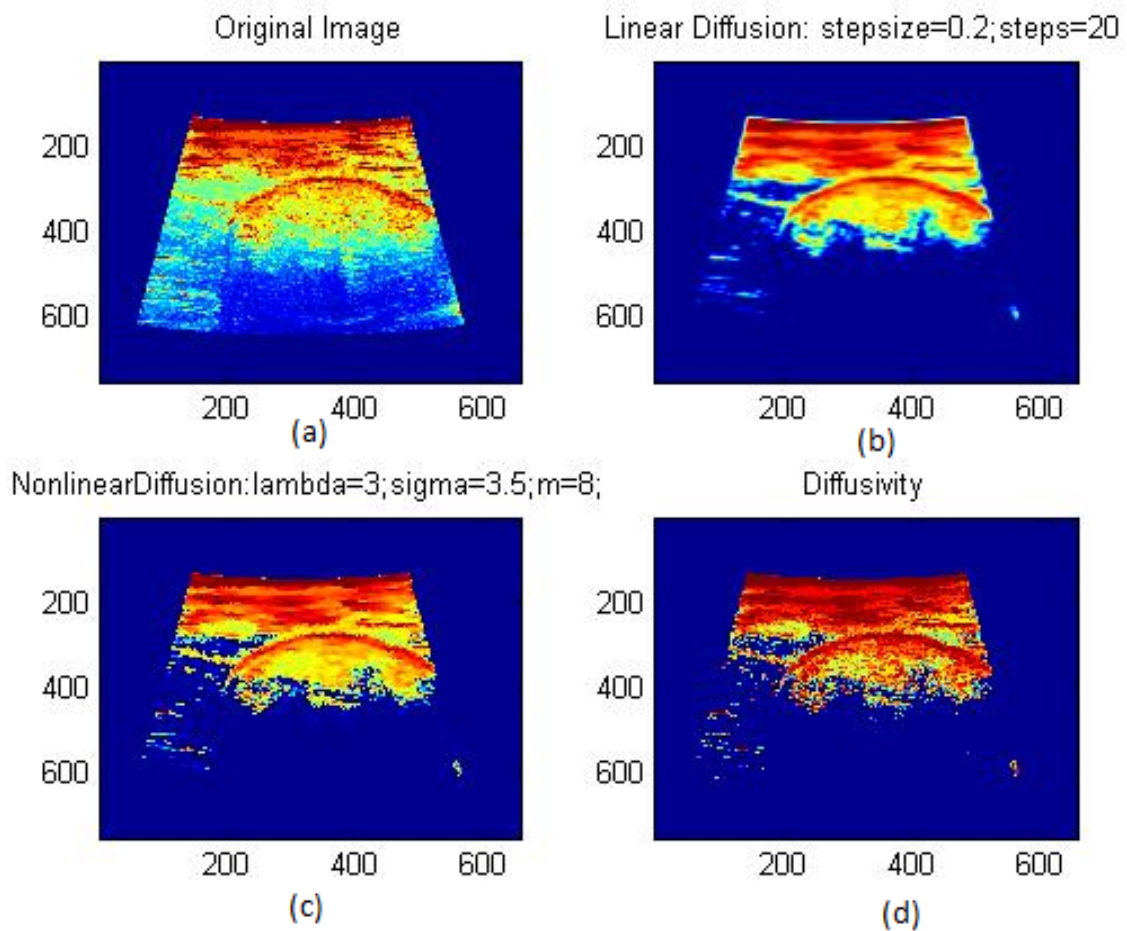


Figure 5.11 Colormap images of the diffusion filter step. (a) Original Image (b) Linear Diffusion (c) Nonlinear Diffusion with (d) Diffusivity used for nonlinear diffusion.

5.3 Connected component analysis

Connected-component analysis is a well understood algorithm, where subsets of connected components are uniquely labeled based on some properties like intensity, area, orientation etc. Any set of pixels which are not separated by a boundary are called connected.

In this thesis work, one might recall that at first a binary image was created using the input US image. Then connected component analysis is performed on this binary image by using an eight-connected neighborhood connectivity (8-connected pixels are neighbors to every pixel that touches one of their edges or corners. These pixels are connected horizontally, vertically, and diagonally. In addition to 4-Connected pixels, each pixel with coordinates $x \pm y$ or $x \mu y$ is connected to the pixel at (x, y)).

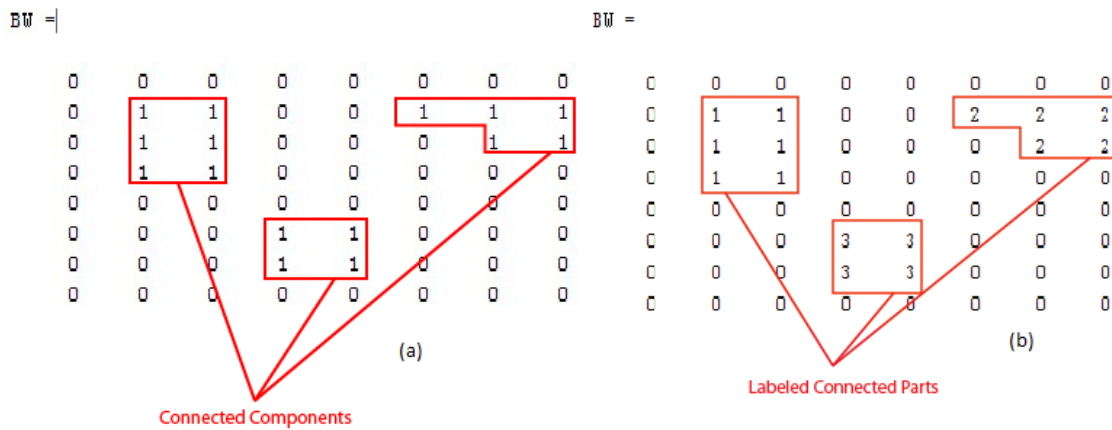


Figure 5.12 (a) Connected components are marked in a binary image (b) Connected components are labeled.

Once region boundaries have been detected, regions are labeled according to the number of pixels (figure 5.12). Thereafter, the algorithm removes all the connected components with fewer than 40 points. The logic for the choice of this number is as follows: Considering that the minimum length of the observed needle is 59.986mm or 170.037 points table 5.1, components with fewer than 40 points can be removed. This can be varied according to the minimum length

of the needle inserted, when the ANDSUI algorithm starts. This binary image is used as a mask for the input image. This helps in removing the staggered components seen in figure 5.10.

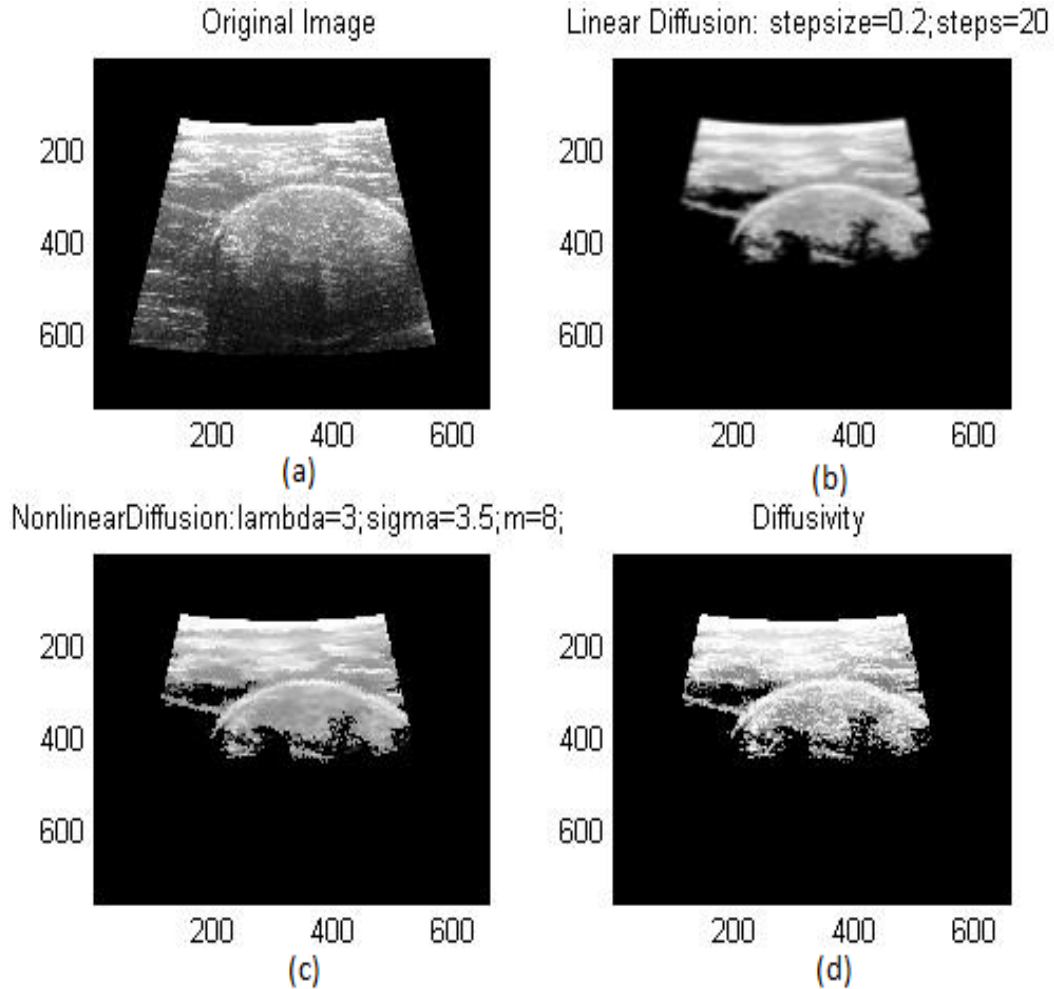


Figure 5.13 Result after applying connected component analysis (a) Original Image (b) Linear Diffusion (c) Nonlinear Diffusion with (d) Diffusivity used for nonlinear diffusion.

5.4 Second order Gaussian filter and morphological closure

In this step, the appearance of the needle in the images is enhanced by first applying morphological closing and then convolving the US images with a second order of Gaussian filter.

5.4.1 Morphological closing

Morphological closing is an operation in which image is first dilated and then eroded. This operation is used to eliminate holes in the image. Dilations is an operation in which neighbors of every white pixel in an original image is made white in the resulting image. It is used for probing and expanding the shapes contained in the input image. Erosion is an operation in which neighbors of every black pixel in original image is made black in the resulting image. Morphological closing is applied to eliminate holes from the distorted needle boundaries. Line is used as a structural element for this process.

5.4.2 Second order Gaussian filter

A second order Gaussian filter is specifically designed for exploiting the tubular structure of the needle and suppressing the imaging noise at the same time. The second order derivative of Gaussian filter is suitable for this work. In 2D, the filter can be formulated as [40]:

$$G''(x, y) = 2 \left(\frac{2x^2 - 1}{\sigma_x} + \frac{2y^2 - 1}{\sigma_y} \right) \exp\left(-\frac{x^2}{\sigma_x} - \frac{y^2}{\sigma_y}\right) \quad (5.1)$$

where σ_x , σ_y are the variation in x, y directions, respectively. While this edge detection is also a well known approach, we customize it for our application. We know that the needle is tubular. To exploit the tubular structure of the needle, the values of σ_x and σ_y are selected in a way that $\sigma_y > \sigma_x$. Figure 5.14 shows the surface of a second order Gaussian filter. The response of the filter is low on the needle and is high at other places.

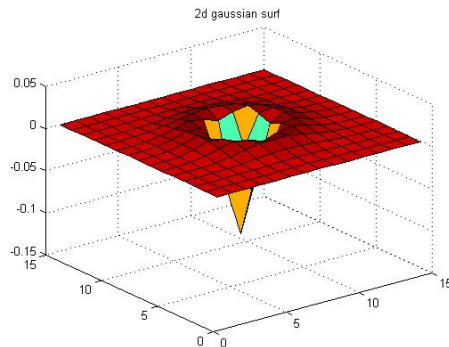


Figure 5.14 Surf of 2nd order Gaussian filter.

5.4.3 Demonstration for results of Morphological closing and 2nd order Gaussian filter

Figure 5.15 shows the result after morphological closing is applied to the US image and then convolved with second derivative of the Gaussian filter. Visually, the needle becomes sharper and the holes are reduced after passing through these two operations.

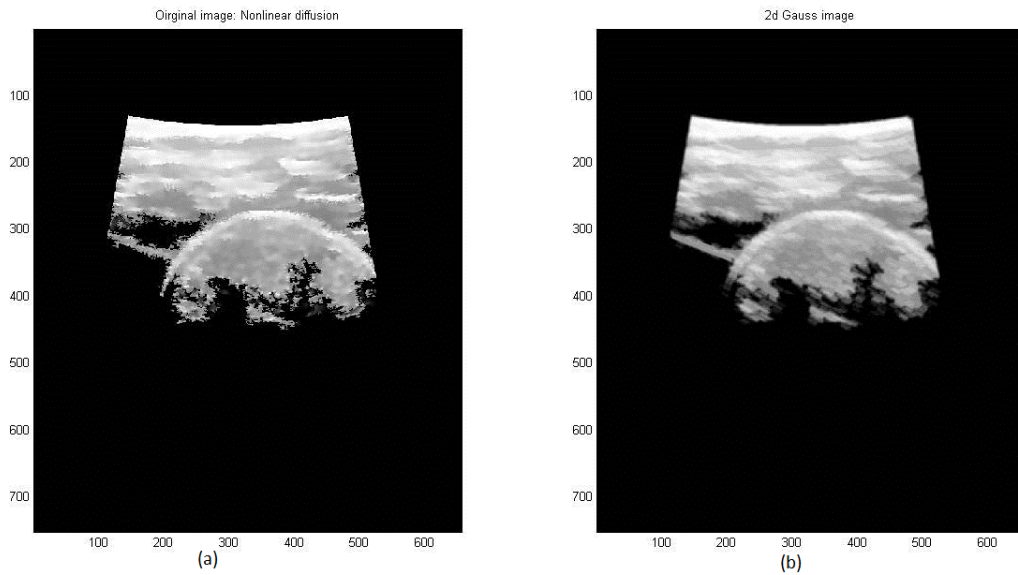


Figure 5.15 Second order Gaussian filter (a) Original image from step nonlinear diffusion (b) Image after passing through the second order Gaussian filter and morphological closure.

5.5 Needle marking using Hough Transform

Finally, the needle is marked using the grayscale Hough Transform described in chapter 3.1. Hough Transform was implemented such that, the range of angle 'θ' (described in chapter 3.1) for the current frame is considered to be $\theta_{\text{current}} \in [\theta_{\text{previous}} - 5^\circ, \theta_{\text{previous}} + 5^\circ]$, where θ_{previous} is the angle of a needle axis segmented in the previous frame and θ_{current} is the angle of a needle axis segmented in the current frame. This approach has two advantages: Computational time for the algorithm reduces as range of angular search is decreased and also needle segmentation can be accomplished in the cases with false markings along with the needle, such as 5.19 (d).

Lines due to image boundary and lines containing less than 20 points are ignored (The minimum length of the observed needle is 59.986mm or 170.037 points - see Table 5.1. So, lines with length less than 20 points can logically be ignored. This can be varied according to the minimum length of inserted needle, when ANDSUI algorithm starts). Section 5.6 shows the results for needle marking using Hough Transform.

5.6 Results and Calculation

Needle segmentation algorithm, described above, is applied on the images shown in figure 5.1 (e), (f) and (g). The Hough Transform step of the ANDSUI algorithm, described in the section 5.5, returns the coordinates of start (x_1, y_1) and end points (x_2, y_2) of the needle axis, shown in table 5.1. Also, the observed needle location is marked on these images (figure 5.17 (c) to 5.19 (c)) and compared with the results of the ANDSUI algorithm.

5.6.1 Angle Calculations

Angle made by the needle axis can be calculated by:

$$\theta_{needle} = \tan^{-1}\left(\frac{y_1 - y_2}{x_1 - x_2}\right) \quad (5.1)$$

And angle deviation can be calculated using:

$$\theta_{deviation} = |\theta_{CalculatedNeedle} - \theta_{ObservedNeedle}| \quad (5.2)$$

5.6.2 Length Calculations

Length of the needle can be calculated by:

$$L_{needle} = \sqrt{((x_1 - x_2)^2 + (y_1 - y_2)^2)} \quad (5.3)$$

And length deviation can be calculated by:

$$L_{deviation} = |L_{CalculatedNeedle} - L_{ObservedNeedle}| \quad (5.4)$$

The length and the length deviation given by equation 5.3 and 5.4 are in unit "point". This can be converted to millimeters using the conversion equation: 1 point = 0.35278 millimeters.

5.6.3 Tip Position Calculations

Needle tip is given by the end point coordinates (x_2, y_2) . Positional deviations for the needle can be calculated as:

$$P = (\sqrt{(x_{2-\text{calculatedNeedle}} - x_{2-\text{ObservedNeedle}})^2 + (y_{2-\text{calculatedNeedle}} - y_{2-\text{ObservedNeedle}})^2}) \quad (5.5)$$

Table 5.1 summarizes the output of algorithm used in this work. The ANDSUI algorithm successfully finds the location of needle with average angle deviation $< 1^\circ$, average length deviation of 2.135 mm and average positional deviation of 3.383mm.

Table 5.1 also mentions the average time taken to execute the algorithm with 5 experimental execution for each case. Time taken can typically be decreased 20 times, in worst case, by converting the matlab code to traditional programming language like C/C++.

Table 5.1 Needle location in terms of angle, length, starting coordinates and ending coordinates for different input images

Figure	Angle (degree)	Length (mm)	X ₁ ,Y ₁ (pt)	X ₂ ,Y ₂ (pt)	Time (Sec)	Angle Deviation	Length Deviation	Positional Deviation (mm)
5.17(c) Observed	179.827	88.099	362, 262	608, 305	-	-	-	-
5.17(d) Calculated	179.859	90.453	362, 264	621, 309	3.79729	0.032	2.354	3.798
5.18(c) Observed	179.831	131.71 1	363, 265	731, 328	-	-	-	-
5.18(d) Calculated	179.798	129.74 2	365,2 64	716, 326	3.55387	0.033	1.971	3.338
5.19(c) Observed	179.788	62.066	363, 263	535, 300	-	-	-	-
5.19(d) Calculated	178.822	59.986	360, 267	527, 297	4.40662	0.966	2.08	3.014
Average					3.939	0.349	2.135	3.383

Figure 5.16 demonstrates the case when step 1 of the ANDSUI algorithm, cropping borders, is not executed. Figure 5.6 (c) shows the segmented needle marked with red color. Clearly, border lines are mistakenly classified as the needle. Infact, the actual needle is not at all classified. So step 1 of the ANDSUI algorithm is necessary for the proper segmentation of the needle.

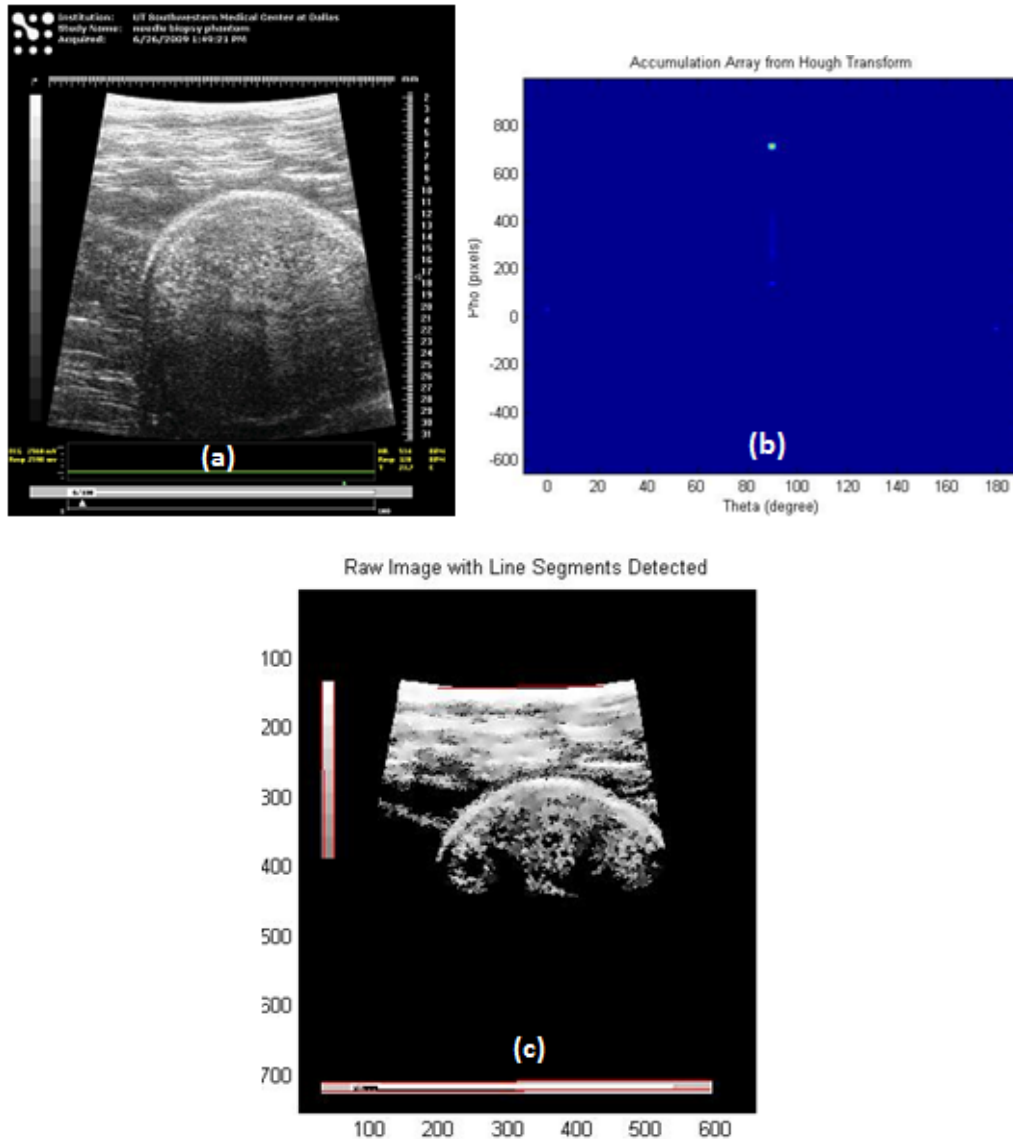


Figure 5.16 False results when borders are not cropped (a) Original image (b) Accumulator array plot of Hough transform (c) Needle segmented marked as red.

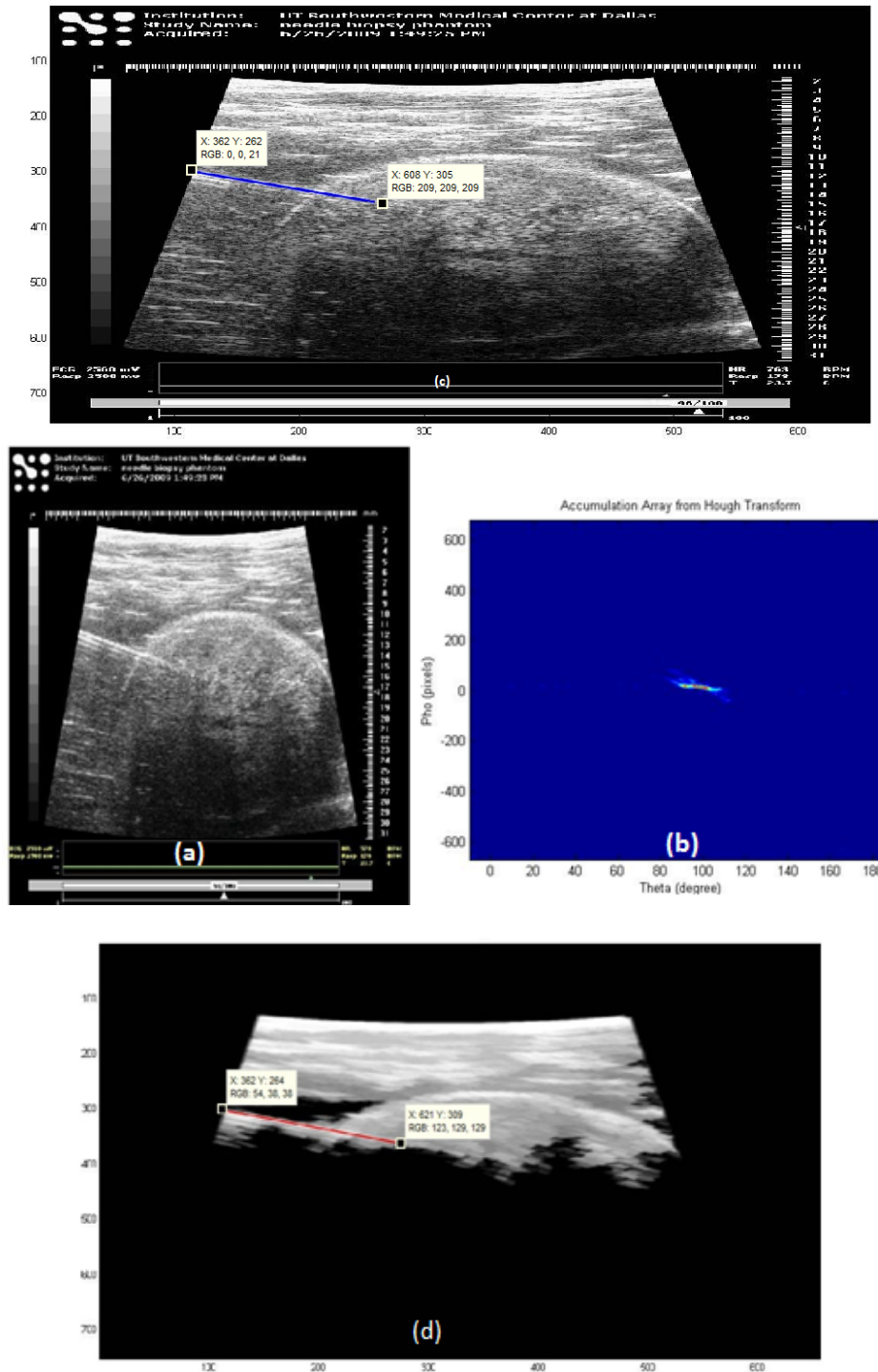


Figure 5.17(a) Original image (b) Accumulator array plot of Hough transform (c) Observed needle (d) Needle segmented marked as red.

Figure 5.17 demonstrates the case when the US image has reverberation artifacts. Figure 5.17 (c) and (d) shows the needle marked by the observer and by the algorithm respectively. The start and the end points are also marked. Table 5.1 show the comparison between these two needle locations in terms of angular, positional and length deviations.

Figure 5.18 demonstrates the case when the brightness of the needle voxels is comparable to the background. Figure 5.18 (c) and (d) shows the needle marked by the observer and by the algorithm respectively. Figure 5.18 (b) shows the bright line in the plot of accumulator corresponding to the needle. Table 5.1 show the comparison between the manually marked needle location and needle location segmented by the ANDSUI algorithm.

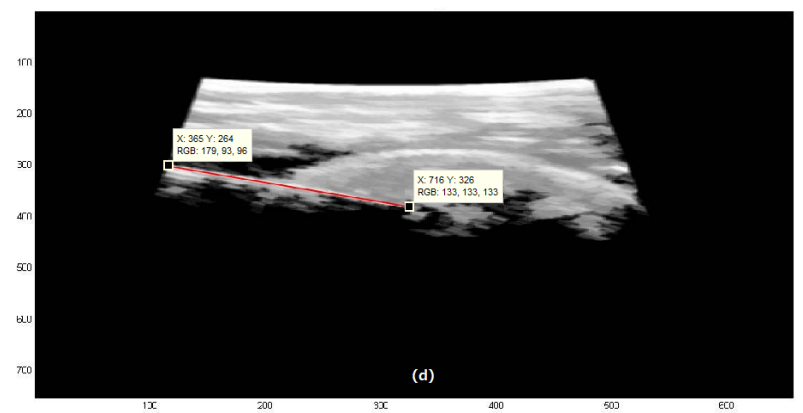
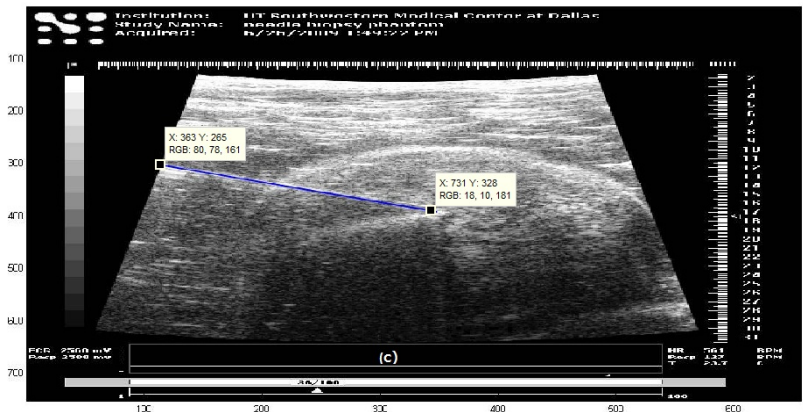
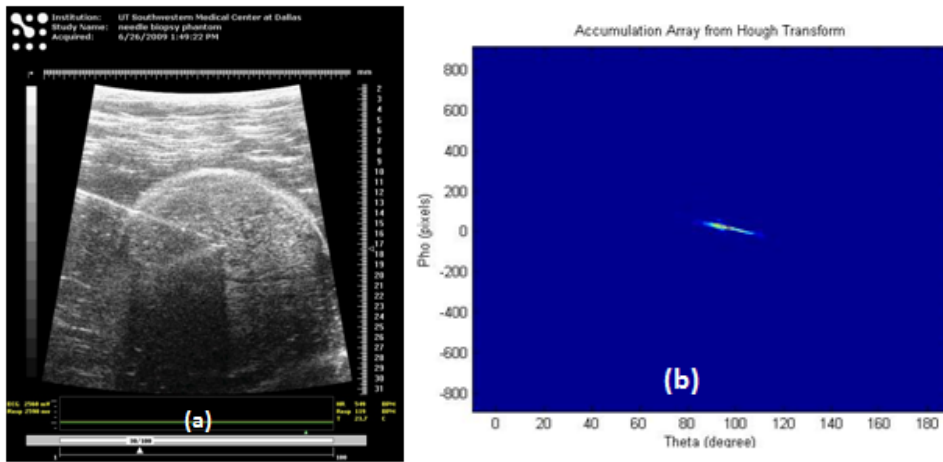


Figure 5.18(a) Original image (b) Accumulator array plot of Hough transform (c) Observed needle (d) Needle segmented marked as red

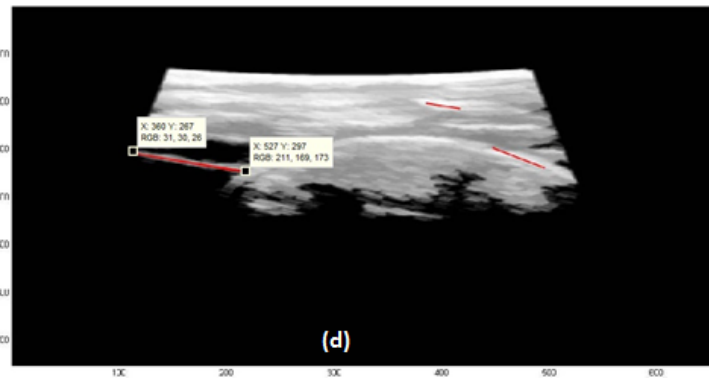
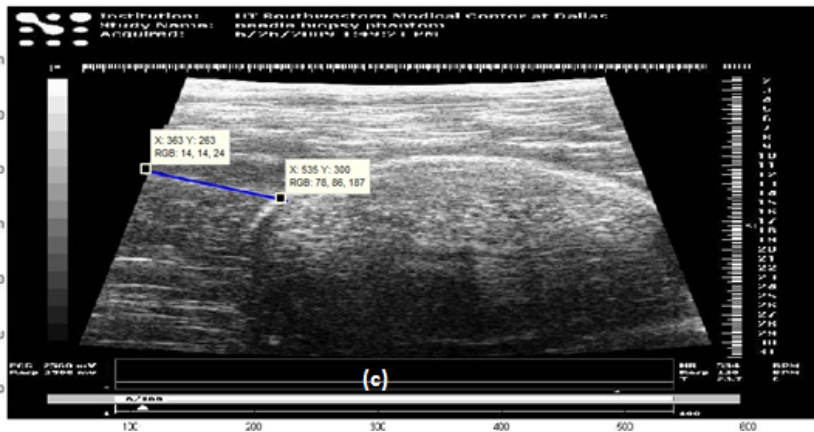
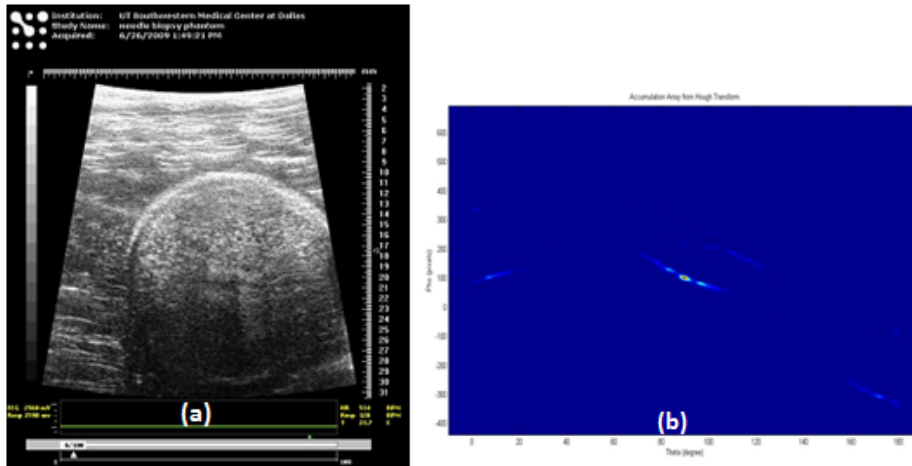


Figure 5.19 (a) Original image (b) Accumulator array plot of Hough transform (c) Observed needle (d) Needle segmented marked as red. There are also some false markings. This is the case when the needle is not bright compared to background due to speckle noise.

Figure 5.19 demonstrates the case when brightness of needle voxels is less compared to the background due to presence of speckle noise. Figure 5.19 (c) and (d) shows the needle marked by the observer and by the algorithm respectively. As shown in figure 5.19 (d), there are some false markings along with the needle. But these false markings can potentially be ignored after considering the information about the needle location from the previous frame. Table 5.1 show the comparison between these two needle locations in terms of angular, positional and length deviations.

Compared to the algorithms discussed in chapter 3, our algorithm has the highest accuracy in angular deviation, 0.349 degrees, among all the algorithms. Also, accuracy in length deviation (2-3 mm) is comparable to these works, even with the speckled US images. Our computational time is also less compared to most of the algorithms discussed above. The ANDSUI algorithm for segmenting needle performs all the calculations on CPU. So, the computational time can be reduced considerably, by taking advantage of parallel processing and using GPU. Also, as mentioned before, this computational time can be reduced 20 times, in worst case, by converting the matlab code to traditional programming language like C/C++. Hence, ANDSUI algorithm can be used for the real time breast biopsy procedures.

The needle axis and tip location calculated from the ANDSUI algorithm is then provided to the path planning block (shown in figure 1.1). If required, this algorithm recreates a new path for the surgeon to follow from the current needle location to the cancer cell location [54]

CHAPTER 6

CONCLUSION AND FUTURE WORK

6.1 Conclusion

The main aim of this thesis is to find the needle axis and tip location in real time, even when the general issues of ultrasound imaging like low spatial resolution due to a large amount of speckle noise, incomplete object structure etc. prevail.

The algorithm described in this thesis reads the US frames one by one from the input video, improves the quality of the image by applying a customized non linear anisotropic diffusion followed by connected component analysis, removes the needle distortions by morphological closure and a second order Gaussian filter and finally, marks the needle axis and tip using an edge detector (Hough Transform).

Also, different types of diffusion filters, based on partial differential equation, are explored and there results are gauged on both real and simulated data sets for improving image quality. Nonlinear anisotropic diffusion filtering is found to be better in the case of edge enhancement for this specific class of US images.

6.2 Future Work

Work mentioned in this thesis primarily works on 2D images. This work can be extended to find the needle location in 3D space by taking a set of orthogonal 2D images and applying the algorithm on each of the 2D images and collating the results in an intelligent fashion.

The ANDSUI algorithm can be converted from MATLAB to the tradition programming languages like C/C++ to make the system more time efficient.

REFERENCES

- [1] M. Barva, "Localization of Surgical Instruments in 3D Ultrasound Images", PhD Thesis CTU–CMP 2007–12, Center for Machine Perception, K13133 FEE Czech Technical University, Prague, Czech Republic, June 2007.
- [2] Rose JS, Ultrasound Physics and Knobology. In Simon BC, Snoey ER, editors. "Ultrasound in Emergency and Ambulatory Medicine." St Louis: Mosby, 1996, p. 10–38.
- [3] M. Ali, D. Magee and U. Dasgupta, "Signal Processing Overview of Ultrasound Systems for Medical Imaging," SPRAB12, Texas Instruments, Texas, November 2008.
- [4] Mark L. Palmeri, "Ultrasound Beamforming and Image Formation", M.D., Ph.D., Biomedical Engineering, Duke University, RSNA 2007
- [5] J C Bamber, "Image Formation and Image Processing in Ultrasound", <http://mpss.iop.org/1999/pdf/bamber.pdf>.
- [6] Richard A. Lopchinsky, MD, FACS and Nancy H. Van Name, RDMS, RTR, and Marlene Kattaron, RDM. "Physical Principles of Ultrasound."
- [7] William A. Steelman, "Comparison of Real-time Scan Conversion Methods With an OpenGL Assisted Method". <http://www.cs.wustl.edu/~jain/cse567-08/ftp/scan/index.html>.
- [8] "Surgical Tool Localization in 3D Ultrasound Data, PhD Thesis Proposal" CTU–CMP–2009–08, Center for Machine Perception, Czech Technical University in Prague, Czech Republic, February 2010. <ftp://cmp.felk.cvut.cz/pub/cmp/articles/uhercik/Uhercik-TR-2009-08.pdf>
- [9] R. O. Duda and P. E. Hart, "Use of the Hough Transformation to Detect Lines and Curves in Pictures." Commun. ACM, 15(1):11–15, 1972.
- [10] Wu Qiu; Mingyue Ding; Ming Yuchi: "Needle Segmentation Using 3D Quick Randomized Hough Transform." Intelligent Networks and Intelligent Systems, 2008. ICINIS '08, p. 449 - 452.

- [11] H. Zhou, W. Qiu, and M. Ding. "Automatic Needle Segmentation in 3D Ultrasound Images Using 3D Hough Transform." In Proceedings of SPIE Medical Imaging, 2007, SPIE 6789, 67890R
- [12] H. Zhou, W. Qiu, M. Ding, and S. Zhang. "Automatic Needle Segmentation in 3D Ultrasound Images Using 3D Improved Hough Transform." In Proceedings of SPIE Medical Imaging, 2008, SPIE 6918, 691821.
- [13] K. S. Roberts. "A New Representation for a Line." In Computer Vision and Pattern Recognition, 1988." Proceedings CVPR '88., Computer Society Conference on, pages 635–640, Jun 1988.
- [14] P. Bhattacharya, H. Liu, A. Rosenfeld, and S. Thompson. "Hough Transform Detection of Lines in 3-d Space." Pattern Recognition Letters, 21(9):843 – 849, 2000.
- [15] L. Xu, E. Oja, and P. Kultanen. "A New Curve Detection Method: Randomized Hough Transform (RHT)." Pattern Recogn. Lett., 11(5):331–338, 1990.
- [16] L. Xu and E. Oja. "Randomized Hough Transform." Encyclopedia of Artificial Intelligence, pages 1354–1361, 2008.
- [17] N. Kiryati, Y. Eldar, and A. M. Bruckstein. "A Probabilistic Hough Transform." Pattern Recogn., 24(4):303–316, 1991.
- [18] K. J. Draper, C. C. Blake, D. B. Gowman, L. nad Downey, and A. Fenster. "An Algorithm for Automatic Needle Localization in Ultrasound-guided Breast Biopsies." Medical Physics, 27:1971–1979, 2000.
- [19] P. M. Novotny, J. W. Cannon, and R. H. Howe. "Tool Localization in 3D Ultrasound Images." In Proceedings of Medical Image Computing and Computer-Assisted Intervention, volume 2879, pages 969–970, 2003.
- [20] Paul M. Novotny, Jeff A. Stoll, Nikolay V. Vasilyev, Pedro J. del Nido, Pierre E. Dupont, Todd E. Zickler and Robert D. Howe. "GPU Based Real-time Instrument Tracking with Three-dimensional Ultrasound."

Volume 11, Issue 5, October 2007, Pages 458-464 Special Issue on the Ninth International Conference on Medical Image Computing and Computer-Assisted Interventions - MICCAI 2006

[21] L. F. Oliveira, D. M. Simpson, and J. Nadal, "Calculation of Area of Stabilometric Signals Using Principle Component Analysis," *Physiol. Meas.* **17**, 305–312 ~1996.

[22] Martin Barva, Jan Kybic, Jean-Martial Mari, Jean René Duhamel, Christian Cachard, and Václav Hlaváč. "Parallel Integral Projection Transform for Electrode Localization in 3d Ultrasound Images." *IEEE Transactions on Ultrasonics, Ferroelectrics and Frequency Control*, 2007.

[23] E. Heitz, P. Perez, and P. Bouthemy, "Multiscale Minimization of Global Energy Functions in Some Visual Recovery Problems," *Comput. Vision, Graphics, Image Process.*, vol. 59, no. 1, pp. 125–134, 1994.

[24] Martin Barva, Jan Kybic, Jean-Martial Mari, Christian Cachard, and Václav Hlaváč. "Automatic Localization of Curvilinear Object in 3D Ultrasound Images." In William F. Walker and Stanislav Y. Emelianov, editors, *Medical Imaging 2005: Ultrasonic Imaging and Signal Processing*, volume 6 of *Progress in Biomedical Optics and Imaging*, pages 455–462, Washington, USA, July 2005. SPIE.

[25] Martin Barva, Jan Kybic, Jean-Martial Mari, Christian Cachard, and Václav Hlaváč. "Localizing Metal Electrode from 3D Ultrasound Data Using Ransac and Intensity Priors." In Jiří Hozman and Peter Kneppo, editors, *IFMBE: Proceedings of the 3rd European Medical and Biological Engineering Conference - EMBEC*, volume 11, pages 1–6, Prague, Czech Republic, November 2005. IFMBE.

[26] P. Perona & J. Malik. "Scale-space and Edge Detection Using Anisotropic Diffusion." *IEEE Transactions on Pattern Analysis and Machine Intelligence* 12, pp. 629–639, 1990.

[27] K. Z. Abd-Elmoniem, A.-B. M. Youssef, and Y. M. Kadah, "Real-time Speckle Reduction and Coherence Enhancement in Ultrasound Imaging Via Nonlinear Anisotropic Diffusion," *IEEE Trans. Biomed. Eng.*, vol. 49, no. 9, pp. 997–1014, Sep. 2002.

- [28] Weickert, J. 1998. "Anisotropic Diffusion in Image Processing." Teubner, Stuttgart.
- [29] Crawford DC, Cosgrove DO, Tohno E, et al. "Visual Impact of Adaptive Speckle Reduction on US B-mode Images." *Radiology* 1992;183:555–61.
- [30] R. F. Wagner and M. F. Insana, "Analysis of Ultrasound Image Texture Via Generalized Rician Statistics," *Proc. SPIE*, vol. 556, pp. 153–159, 1985.
- [31] J. W. Weickert, B. M. Romney & M. A. Viergever. "Efficient and Reliable Schemes for Nonlinear Diffusion Filtering." *IEEE Transactions on Image Processing* 7, pp. 398–410, 1998.
- [33] Bogdan J Matuszewski, Mahbubunnabi Tamal, Gareth Price and Christopher J. Moore "Diffusion Filters for Structured Noise Removal" Univeristy of Central Lancashire, Preston, UK <http://www2.wiau.man.ac.uk/caws/Conferences/46/proceedings/papers/MIUAdiffusionpaper.pdf>
- [34] A.P. Witkin, "Scale-space Filtering", *Proc. Eighth Int. Joint Conf. on Artificial Intelligence (IJCAI '83, Karlsruhe, Aug. 8–12, 1983)*, Vol. 2, 1019–1022, 1983.
- [35] E.S. Posmentier, "The Generation of Salinity Finestructure by Vertical Diffusion", *J. Phys. Oceanogr.*, Vol. 7, 298–300, 1977.
- [36] F. Catt'e, P.-L. Lions, J.-M. Morel, T. Coll, "Image Selective Smoothing and Edge Detection by Nonlinear Diffusion," *SIAM J. Numer. Anal.*, Vol. 29, 182–193, 1992.
- [37] Weickert, J. 1995. "Multiscale Texture Enhancement", *Computer analysis of images and patterns, Lecture Notes in Comp. Science, 970*, Springer, Berlin, pp. 230–237.
- [38] J. Weickert, "Theoretical Foundations of Anisotropic Diffusion in Image Processing," *Computing*, Suppl. 11, 221–236, 1996.
- [39] Weeratunga S.K., and C. Kamath, "A Comparison of PDE-based Nonlinear Anisotropic Diffusion Techniques for Image Denoising," *Proceedings, Image Processing: Algorithms and Systems II, SPIE Electronic Imaging, San Jose, January 2003*.
- [40] Alper Ayvaci, Pingkun Yan, Sheng Xu, Stefano Soatto, Jochen Kruecker, "Biopsy Needle Detection in Transrectal Ultrasound", *Computerized Medical Imaging and Graphics* Volume 35, Issues 7-8, October-December 2011, Pages 653-659.

- [41] A. Abati and A. Simsir, "Breast Fine Needle Aspiration Biopsy: Prevailing Recommendations and Contemporary Practices," *Clin. Lab. Med.*, vol. 25, no. 4, pp. 631–654, Dec. 2005.
- [42] K. Kern, "Sentinel Lymph Node Mapping in Breast Cancer Using Subareolar Injection of Blue Dye," *J. Amer. College Surg.*, vol. 189, no. 6, pp. 539–545, Dec. 1999.
- [43] N. Abolhassani, R. Patel, and M. Moallem, "Needle Insertion into Soft Tissue: a Survey," *Med. Eng. Phys.*, vol. 29, no. 4, pp. 413–431, 2007.
- [44] V. Horsley and R. H. Clarke, "The Structure and Functions of the Cerebellum Examined by a New Method," *Brain*, vol. 31, pp. 45–124, 1908.
- [45] M. Felber. "Optical Measurement System for Medical Applications." PhD thesis, Swiss Federal Institute of Technology, Lausanne, Switzerland, 2002.
- [46] T. M. Peters, "Image-guidance for Surgical Procedures," *Phys. Med. Biol.*, vol. 51, no. 14, pp. R505–R540, 2006
- [47] Women's Health, <http://women.webmd.com/guide/breast-cancer-arm-yourself-with-facts>
- [48] National Cancer institute, <http://www.cancer.gov/cancertopics/types/breast>
- [49] http://www.polyurethane.org/s_api/sec.asp?CID=884&DID=3560, Centre for the Polyurethane studies.
- [50] Y. Yu and S. T. Acton, "Speckle Reducing Anisotropic Diffusion," *IEEE Trans. Image Process.*, vol. 11, no. 11, pp. 1260–1270, Nov. 2002.
- [51] A. Achim, A. Bezerianos, and T. P., "Novel Bayesian Multiscale Method for Speckle Removal in Medical Ultrasound Images," *IEEE Trans. Med. Imag.*, vol. 20, no. 8, pp. 772–783, Aug. 2001.
- [52] Kaur, A. and Singh, K. (2010), "Speckle Noise Reduction by Using Wavelets," NCCI 2010 - National Conference on Computational Instrumentation CSIO, Chandigarh, INDIA, pp. 198-203.

[53] B. Svensson, "A Multidimensional filtering Framework with Applications to Local Structure Analysis and Image Enhancement," Ph.D. dissertation, Linkoping University, Sweden, April 2008.

[54] Sridhar Rajaram, Optimal Path Planning, Implementation and Simulation for a Breast Biopsy System, Master's Thesis, University of Texas at Arlington, December 2011.

BIOGRAPHICAL INFORMATION

Nidhi Khullar was born on 15th August, 1985 in Delhi, India. She completed her Bachelor of Technology in Electronics and Communication Engineering from Guru Gobind Singh Indraprastha University, New Delhi in May 2007. She worked as a Software Engineer at Adobe systems India from 2007-2008. She obtained her Master of Science degree from the University of Texas at Arlington in December 2011. She worked for Ericsson as an intern in spring and summer of 2010, where she worked on developing embedded software for an LTE modem. Her current research interests include image processing and embedded software development.